JMEPEG (2020) 29:6535–6549
https://doi.org/10.1007/s11665-020-05176-z

1059-9495/$19.00

Electrochemical Behavior of Cobalt Oxide/Boron-Incorporated Reduced Graphene Oxide Nanocomposite Electrode for Supercapacitor Applications

R. Naresh Muthu and Sankara Sarma V. Tatiparti

(Submitted April 30, 2020; in revised form September 3, 2020; accepted September 27, 2020)

Electrodes from hydrothermally synthesized boron-incorporated reduced graphene oxide (B-rGO), Co_3O_4, and Co_3O_4/B-rGO nanocomposites are tested in 2 M KOH and NaOH electrolytes for supercapacitor applications. Structural characterization was done by x-ray diffraction and x-ray photoelectron spectroscopy. Cyclic voltammogram of B-rGO indicates partial electrical double-layer capacitance and pseudocapacitive behaviors. Co_3O_4, shows two reversible redox peaks, indicating diffusion-controlled (battery-like) process. Interestingly, Co_3O_4/B-rGO possesses both the pseudocapacitive and diffusion-controlled features. The specific capacitance (C_{sp}) from galvanostatic charge/discharge experiments is higher in all the electrodes in KOH than in NaOH. Co_3O_4/B-rGO shows the highest C_{sp} of 600 F g^{-1} (270 C g^{-1}) at 0.1 A g^{-1} and 454 F g^{-1} (204 C g^{-1}) at 10 A g^{-1} in KOH. Co_3O_4/B-rGO-KOH system retains 87.8% capacitance after 2000 cycles, demonstrating very good cyclic stability. Co_3O_4/B-rGO-KOH system yields, a remarkable, maximum power density of 2250 W kg^{-1} with an energy density of 12.77 W h kg^{-1} at 10 A g^{-1}. The better performance in KOH is attributed to the low hydration sphere radius, high ionic conductivity of K^+, low diffusive and charge transfer and electrode resistance, estimated from electrochemical impedance spectroscopy. The electrode–electrolyte combination is crucial for the overall performance as a supercapacitor electrode.

Keywords battery-like, B-rGO, Co_3O_4/B-rGO, cobalt oxide, EDLC, supercapacitor

1. Introduction

The depletion of fossil fuels and increasing energy demand have triggered research in alternative energy and power sources. Supercapacitors can yield high power density and possess long cyclic stability (Ref 1). They are classified broadly into two types based on the charge storage mechanism: (i) non-Faradaic (i.e., electrical double-layer capacitors or EDLCs) and (ii) Faradaic (i.e., diffusion-controlled or battery-like involving reversible redox reactions) (Ref 2, 3).

Carbon-based materials, viz. activated carbon (Ref 4), carbon nanotubes (Ref 5, 6), carbon nanofiber (Ref 7) and graphene (Ref 8, 9), are used as EDLC electrodes because of their high surface area and tunable surface properties (Ref 4-11). For example, the activated carbon synthesized from cap and stalk of mushrooms through microwave-induced method resulted in a specific capacitance (C_{sp}) 271.94 and 269.66 F g^{-1} at 0.5 A g^{-1} (Ref 12). The power density and cycle life of these EDLCs are excellent. However, they suffer from poor energy density as the charge storage in them is limited by the pure electrostatic charge accumulation on the surface (Ref 13, 14). The energy density of these carbon-based materials can be largely improved and expanded after doping with heteroatoms such as nitrogen (N) (Ref 15), boron (B) (Ref 16, 17), sulfur (S) (Ref 18) and phosphorus (P) (Ref 19), which can tailor the electronic properties of the carbon-based materials (Ref 17, 20). For example, in our recent study, we synthesized reduced graphene oxide (rGO) from electrochemical exfoliation, which exhibited only 9.86 W h kg^{-1} (Ref 20). Interestingly, upon boron incorporation the obtained material (B-rGO) showed an energy of 25.2 W h kg^{-1} at 20 A g^{-1} (Ref 20). This was attributed to the *p*-doping effect caused by the electron deficient B into rGO due to the absence of π electrons (Ref 16, 20).

Metal oxides, viz. Co_3O_4 (Ref 21-24), NiO (Ref 25, 26), Fe_2O_3 (Ref 27), MnO_2 (Ref 28, 29) and RuO_2 (Ref 30), can store charge Faradaically by ionic insertion through reversible redox reactions (Ref 21-31). The transition-metal oxides such as RuO_2 (Ref 30), MnO_2 (Ref 28), Co_3O_4 (Ref 21-24), NiO (Ref 25), IrO_2 (Ref 32) and V_2O_5 (Ref 33) have higher charge storage capacities than the carbon-based EDLCs due to the redox reactions. For example, the low-cost cobalt oxide (Co_3O_4) possesses high theoretical C_{sp} (3560 F g^{-1}), high stability and lower toxicity (Ref 21-24). Well-crystalline porous Co_3O_4 nanorods synthesized through hydrothermal method by Jang et al. (Ref 22) showed a C_{sp} of 316.4 C g^{-1} at 10 mV s^{-1} of scan rate during cyclic voltammetry. In another study, Wang et al. prepared Co_3O_4 nanostructures with a C_{sp} of 35 4.6 C g^{-1} at 0.5 A g^{-1} (Ref 23). Feather-like Co_3O_4 electrode exhibits a high C_{sp} of 396.67 F g^{-1} (Ref 24). One of the main reasons for

Electronic supplementary materialThe online version of this article (https://doi.org/10.1007/s11665-020-05176-z) contains supplementary material, which is available to authorized users.

R. Naresh Muthu and **Sankara Sarma V. Tatiparti**, Department of Energy Science and Engineering, Indian Institute of Technology Bombay, Mumbai, Maharashtra 400076, India. Contact e-mail: sankara@iitb.ac.in.

such high C_{sp} in Co_3O_4 is due to the multivalence of Co ions. During potential sweeping, Co^{2+} and Co^{3+} present in Co_3O_4 get reversibly converted to Co^{3+} and Co^{4+}, respectively, due to two sets of redox reactions (Ref 34, 35). The practical C_{sp} of Co_3O_4 can be increased further by providing sufficient means of better ionic insertion through electrolyte modification and incorporating synergy in charge storage by combining with EDLCs.

The Co_3O_4/graphene composites have become highly promising electrode materials for high-performance supercapacitors (Ref 36, 37). Many approaches are available for synthesizing the Co_3O_4/graphene composites for the charge storage performance. For example, Guan et al. (Ref 38) prepared needle-like Co_3O_4 anchored on the graphene nanosheets by hydrothermal route. The obtained Co_3O_4/graphene nanosheets exhibit a C_{sp} of 157.7 F g^{-1} at 0.1 A g^{-1}. In another study, He et al. (Ref 39) synthesized Co_3O_4 anchored on RGO nanosheets via hydrothermal method, which showed a C_{sp} 430 F g^{-1} at 1 A g^{-1}. Ma et al. (Ref 40) reported that Co_3O_4 porous nanosheets combined with rGO via refluxing method followed by a thermal annealing process exhibited a high C_{sp} of 518.8 F g^{-1} at 0.5 A g^{-1}. Xie et al. (Ref 41) reported the Co_3O_4/RGO via co-precipitation reaction method with high C_{sp} of 636 F g^{-1} at 1 A g^{-1}. Similarly, the Co_3O_4/RGO nanocomposites prepared through a chemical route possessed a C_{sp} of 784 F g^{-1} at 1 A g^{-1} (Ref 21). Xuan et al. prepared cobalt metal–organic framework (Co-MOF) by solvothermal route which exhibited C_{sp} of 952.5 F g^{-1} at 0.25 A g^{-1} (Ref 42). Ramachandran et al. synthesized Co-MOF, which exhibited the highest capacitance up to 958.1 F g^{-1} at 0.2 A g^{-1} (Ref 43). Xuan et al. reported that a Co-MOF electrode achieved a C_{sp} of F g^{-1} at 0.2 A g^{-1} (Ref 44). Ramachandran et al. reported a maximum C_{sp} of 2872.5 F g^{-1} for the synthesized Co-MOF@Ni electrode (Ref 45). Most of these studies are done at low current densities from around 0.1 to 1 A g^{-1}. At high current densities, usually the charge storage by active materials diminishes due to the increased demand for storing charge in a very small time. The challenge is to synthesize a novel metal oxide—EDLC composite which can show improved performance even at high current densities in a suitable electrolyte system.

In this work, we report the electrochemical behavior of the novel Co_3O_4/B-rGO nanocomposite electrode in both 2 M KOH and 2 M NaOH electrolytes. B-rGO, Co_3O_4 and Co_3O_4 anchored on B-rGO (i.e., Co_3O_4/B-rGO) are synthesized by a facile hydrothermal process. Their electrochemical behavior and performance are tested through cyclic voltammetry (CV); galvanostatic charge/discharge (GCD) at various current densities from 0.1 A g^{-1} to a high value of 10 A g^{-1}. Interestingly, the Co_3O_4/B-rGO electrode demonstrated a remarkable C_{sp} of 600 F g^{-1} (270 C g^{-1}) at 0.1 A g^{-1} and 454 F g^{-1} (204 C g^{-1}) at 10 A g^{-1} in 2 M KOH. The Co_3O_4/B-rGO-KOH system shows 87.8% capacitance retention after 2000 cycles, demonstrating very good cyclic stability. The Co_3O_4/B-rGO-KOH system also yields, a remarkable, maximum power density of 2250 W kg^{-1} with an energy density of 12.77 W h kg^{-1} at 10 A g^{-1}. The performance (i.e., C_{sp}, power and energy density, cycling stability, capacitance retention) of Co_3O_4/B-rGO is the best among all the electrodes tested. The electrochemical performance of all the electrodes is, consistently, better in KOH than in NaOH. The better performance in KOH is attributed to the low hydration sphere radius, high ionic conductivity of K^+, low diffusive and charge transfer and electrode resistance, estimated from electrochemical impedance spectroscopy (EIS). The present work shows that electrode–electrolyte combination is crucial for the overall performance as a supercapacitor electrode.

2. Experimental Section

2.1 Materials

High purity graphite rods (99.9995%, 3.05 mm diameter and 305 mm long) and polyvinylidene fluoride (PVDF) were procured from Alfa Aesar. Cobalt nitrate ($Co(NO_3)_2.6H_2O$, 99%), urea ($CO(NH_2)_2$), potassium hydroxide (KOH), sodium hydroxide (NaOH) and *N*-methyl-2-pyrrolidone (NMP) were purchased from Merck. Carbon black was obtained from Sigma-Aldrich. All purchased chemicals were of analytical grade and used in as received condition without any further purification. Deionized (DI) water was used throughout this study.

2.2 Synthesis of B-rGO

Reduced graphene oxide (rGO) was synthesized from graphite rod by electrochemical exfoliation as reported in our earlier study (Ref 20). For B-rGO synthesis (Ref 46), 0.1 g of the exfoliated rGO was homogenously dispersed in distilled water by ultrasonication for 30 min. The rGO dispersion was added to a solution of 1.5 g of boric acid in 20 ml of DI water and stirred for 30 min for homogenization. The resulting solution was transferred into a Teflon-lined stainless steel autoclave of 100 ml capacity and heated in hot air oven at 150 °C for 12 h. After cooling to room temperature, a black precipitate was obtained, which was collected by centrifugation (REMI, Model: PR-24) and washed with distilled water and ethanol. Finally, it was dried in hot air oven at 60 °C for overnight.

2.3 Synthesis of Co_3O_4/B-rGO

The cobalt oxide anchored on boron-incorporated reduced graphene oxide (Co_3O_4/B-rGO) nanocomposite was synthesized by annealing treatment following a simple hydrothermal method (Ref 39, 47). In a typical experiment, 0.1 M of Co $(NO_3)_2{\cdot}6H_2O$ and 0.1 M of urea were dissolved in 80 ml distilled water. After stirring this solution for 30 min, the synthesized B-rGO was added and the mixture was stirred for 30 min. Eventually, the mixture was transferred to the Teflon-lined stainless steel autoclave, which was used for B-rGO synthesis. The autoclave containing the mixture was then sealed and kept in hot air oven at 180 °C for 12 h. After cooling to room temperature, a sediment was observed in the autoclave, which was collected by centrifugation and washed with water and ethanol several times in that order. The obtained product was dried in hot air oven at 60 °C for 12 h. Finally, a powder was obtained, which was annealed in a muffle furnace at 350 °C for 2 h with a slow heating rate of 5 °C min^{-1} to get the pure Co_3O_4 phase anchored to B-rGO (i.e., Co_3O_4/B-rGO). Pure Co_3O_4 was also synthesized in the similar lines for comparison of its electrochemical behavior with Co_3O_4/B-rGO.

2.4 Preparation of Working Electrodes

B-rGO, Co_3O_4 and Co_3O_4/B-rGO nanocomposite electrodes were prepared. A platinum disk (Pt, 2 mm diameter) was polished with alumina (1.0 μm) slurry on BAINPOL® METCO

polishing machine until a mirror finish was obtained. Following polishing, the electrodes were rinsed with double-distilled water to remove any residual alumina particles. Eventually, the mirror-polished electrodes were sonicated in absolute ethanol followed by double-distilled water for ~10 min. The electrodes were prepared by dispersing 80 wt.% as-prepared B-rGO or Co_3O_4 or Co_3O_4/B-rGO powder, 15 wt.% carbon black and 5 wt.% PVDF binder in NMP using ultrasonication to produce a homogeneous suspension. Then, 10 µl of the suspension was dropped on a cleaned mirror-polished platinum electrode with the help of a micropipette (Sartorius Proline® pipette) and the solvent was evaporated by drying at 60 °C in a hot air oven.

2.5 Structural Characterization

Phase analysis, crystal structure and lattice parameters of the synthesized B-rGO, Co_3O_4 and Co_3O_4/B-rGO nanocomposites were analyzed by x-ray diffraction (XRD, PANalytical EMPYREAN) with a Cu Kα radiation (λ=1.5406 Å) in the 2θ range from 10° to 80°. The elemental composition and oxidation states of metal ions were examined by x-ray photoelectron spectroscopy (XPS, Axis Supra photoelectron spectrometer, Kratos Analytical) using Al Kα as x-ray source (75 W, *hv*: 1486.6 eV) with a pass energy of 20 eV. The synthesized samples of B-rGO, Co_3O_4 and Co_3O_4/B-rGO were ultrasonicated in ethanol and were drop-cast onto an aluminum foil to obtain a thin film, which was eventually dried at 120 °C in a hot air oven for 6 h prior to XPS measurements to minimize the physically observed water (Ref 20). The high-resolution B 1*s*, C 1*s* and Co 2*p* peaks obtained were deconvoluted by subtracting the baseline and fitting using Gauss peak function in Origin Pro 2016 software.

2.6 Electrochemical Measurements

The electrochemical properties of the synthesized B-rGO, Co_3O_4 and Co_3O_4/B-rGO nanocomposite electrodes were studied using CHI 660E electrochemical workstation (CH instruments). The electrochemical experiments were performed in a three-electrode system in two different aqueous electrolytes of 2 M KOH and 2 M NaOH solutions. Cyclic voltammetry (CV), galvanostatic charge/discharge (GCD) and electrochemical impedance spectroscopy (EIS) measurements were carried out. The active material (i.e., B-rGO or Co_3O_4 or Co_3O_4/B-rGO)-coated Pt disk was used as the working electrode. A Pt mesh and saturated calomel electrode (SCE) were used as the counter and the reference electrode, respectively.

Prior to any electrochemical measurement, open circuit potential (OCP) was measured for 1 h to obtain a stable value. CV was performed at various scan rates from 10 to 200 mV s^{-1} in a potential window from −0.10 to 0.50 V versus SCE. GCD tests were conducted in a potential window from −0.05 to 0.40 V versus SCE at current densities from 0.1 to 10.0 A g^{-1}. EIS was conducted at OCP with an amplitude of 10 mV in a frequency range of 1 mHz to 10 kHz. The obtained impedance curves were fitted using ZSimpWin 3.21 software to obtain a suitable model equivalent circuit. Eventually various parameters, viz. solution and charge transfer resistances, were estimated.

3. Results and Discussion

3.1 Structural Analysis

The XRD patterns of the synthesized B-rGO, Co_3O_4 and Co_3O_4/B-rGO nanocomposites are shown in Fig. 1. In Fig. 1, the XRD pattern of B-rGO possesses two peaks around 2θ= 26.55° and 54.6°, corresponding to 002 and 004 planes of graphene, respectively (Ref 20). The appearance of 002 peak at 26.55° in B-rGO corresponds to the interlayer spacing of 3.3574 Å. This spacing indicates that boron (B) is incorporated into rGO as confirmed in our earlier work (Ref 20) and also agrees well with literature (Ref 48). In the XRD patterns of Co_3O_4, and Co_3O_4/B-rGO samples, the diffraction peaks at 2θ =19.0, 31.3, 36.9, 38.5, 44.8, 55.7, 59.4 and 65.2° correspond to 111, 220, 311, 222, 440, 422, 511 and 440 reflections of the face-centered cubic Co_3O_4 (space group 227, Fd $\bar{3}$m; JCPDS card: 42-1467), respectively. The sharp diffraction peaks of Co_3O_4 indicate that it is well crystallized. Peaks corresponding to B-rGO can also be seen in the XRD patterns of Co_3O_4/B-rGO nanocomposites. No characteristic peaks of secondary phases are detected in the XRD patterns, suggesting that single-phase Co_3O_4 is pure and anchored on B-rGO sheets. The crystallite size of Co_3O_4 was estimated by using Debye–Scherrer formula, given in Eq 1 (Ref 49), where *D*: crystalline size, λ: wavelength of x-rays, β: full width at half-maximum of the diffraction peak, and θ: Bragg diffraction angle. The estimated crystallite sizes of Co_3O_4 are 13 nm in pure Co_3O_4 sample and 9 nm in the Co_3O_4/B-rGO nanocomposite. Thus, anchoring Co_3O_4 to B-rGO resulted in a decrease in the average crystallite size of Co_3O_4.

$$D = \frac{0.9\lambda}{\beta \cos\theta} \quad \text{(Eq 1)}$$

Figure 2(a) shows the XPS survey spectra of B-rGO, Co_3O_4 and Co_3O_4/B-rGO in the binding energy range from 50 to 900 eV. The survey spectrum of Co_3O_4 shows peaks corresponding to C 1*s* (284.4 eV), Co 2*p* (780.2 and 795.5 eV) and O 1*s* (532.5 eV). The C 1*s* peak indicates the presence small amount of carbon in Co_3O_4, due to the incomplete burning of ($CO(NH_2)_2$) during Co_3O_4 synthesis (Ref 21). The XPS spectrum of B-rGO exhibits the peaks corresponding to C 1*s* and O 1*s* and B 1*s* (192.4 eV). The spectrum of Co_3O_4/B-rGO exhibits peaks corresponding to B 1*s*, C 1*s*, O 1*s* and Co $2p_{3/2}$ (780.2 eV) and Co $2p_{1/2}$ (795.5 eV). A quantitative estimation from XPS data of Co_3O_4/B-rGO suggests that ~11 at.% of Co_3O_4 is loaded on B-rGO.

The high-resolution XPS spectra of Co 2*p*, C1*s* and B 1*s* corresponding to Co_3O_4/B-rGO nanocomposite are shown in Fig. 2(b), (c) and (d), respectively. Those of C 1*s* and B 1*s* of B-rGO are shown in Figure S1(a) and (b), respectively. The spectrum of Co 2*p* pertaining to Co_3O_4 is shown in Figure S1 (c). The Co 2*p* spectra of Co_3O_4/B-rGO nanocomposite (Fig. 2b) and Co_3O_4 (Figure S1c) show two spin–orbit doublets containing both high energy band Co $2p_{1/2}$ and low energy band Co $2p_{3/2}$ at 795.5 and 780.2 eV, respectively (Ref 50, 51). The binding energy difference between Co $2p_{1/2}$ and Co $2p_{3/2}$ is ~15.3 eV. The spectrum indicates the presence of both Co^{2+}

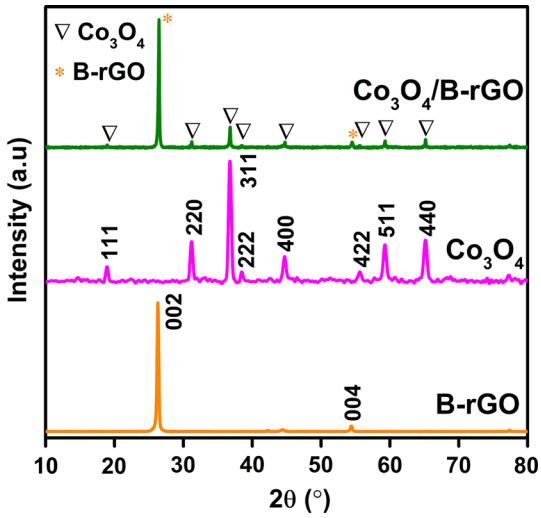

Fig. 1 XRD patterns of B-rGO, Co_3O_4 and Co_3O_4/B-rGO

and Co^{3+} ions corresponding to single-phase Co_3O_4 formation on the surface of B-rGO, which is consistent with the appearance of the peaks corresponding to only Co_3O_4 in XRD (Fig. 1). The satellite peaks (denoted as "sat" in Fig. 2b) at 786.90 and 803.6 eV correspond to Co^{2+} and those at 790.1 and 805.9 eV correspond to Co^{3+} cations, which occupy the tetrahedral and octahedral sites, respectively, in Co_3O_4 unit cell (Ref 50, 52).

The deconvoluted C 1*s* (Figure S1a) spectra of B-rGO and Co_3O_4/B-rGO nanocomposite (Fig. 2c) show five distinguishable peaks at 283.9, 284.7, 285.4, 286.2 and 288.7 eV. The most intense peak at 284.7 eV indicates that the majority of C atoms are arranged in C–C sp^2 hybridization leading to honeycomb lattice structure in both B-rGO and Co_3O_4/B-rGO nanocomposite (Ref 20, 52). The other peaks at higher binding energies (i.e., 285.4, 286.2 and 288.7 eV) correspond to C–OH, C=O and O=C–OH functional groups present in these samples (Ref 53). Interestingly, the peak at 283.9 eV is indicates the C–B bond formation, suggesting the B incorporation into the carbon network of rGO (Ref 17, 20).

The high-resolution B 1*s* spectra of Co_3O_4/B-rGO nanocomposite (Fig. 2d) and B-rGO (Figure S1b) and depict three peaks at 191.2, 192.7 and 193.8 eV, which correspond to the BC_3, BC_2O and BCO_2 (Ref 54). These peaks suggest that B atoms are bonded in various configurations to rGO. Also, interestingly, the presence of BC_3 confirms that B is incorporated into rGO in both B-rGO and Co_3O_4/B-rGO nanocomposites (Ref 20).

3.2 Electrochemical Performance of the Electrodes

Electrochemical performance of the synthesized B-rGO, Co_3O_4 and Co_3O_4/B-rGO is analyzed by CV, GCD and EIS using two different aqueous electrolytes, viz. 2 M KOH and 2 M NaOH solutions (Fig. 3, 4, 5, 6, 7, 8 and Figure S2–S7).

3.2.1 Cyclic Voltammetry. The CVs of the synthesized B-rGO, Co_3O_4 and Co_3O_4/B-rGO in 2 M KOH and 2 M NaOH aqueous electrolyte solutions are presented in Fig. 3(a) and 4 (a), respectively, at a scan rate of 20 mV s^{-1}. The CVs of B-rGO (Fig. 3a and 4a) are almost featureless without any redox peaks, exhibiting partial electrical double-layer capacitive nature (EDLC) through non-Faradaic charging/discharging process and pseudocapacitive nature (Ref 20). On the other hand, the CV from Co_3O_4 electrode exhibits a pair of oxidation (A1 and A2) and reduction peaks (C1 and C2), indicating the typical battery-like nature (Fig. 3a and 4a) (Ref 35). The featureless region (with nonzero current density) is minimal in the case of Co_3O_4. The two sets of redox peaks can be ascribed to the reversible transition of the ions Co^{2+} and Co^{3+} (From XPS, Fig. 2b) to Co^{3+} and Co^{4+} (i.e., $Co^{2+} \leftrightarrow Co^{3+}$ and $Co^{3+} \leftrightarrow Co^{4+}$), respectively (Ref 34, 35). The corresponding reversible reactions are due to the transitions between Co_3O_4 and CoOOH (A1/C1, Fig. 3a) and between CoOOH and CoO_2 (A2/C2, Fig. 3a) (Ref 34, 35, 55), as shown in Eq 2 (Ref 34, 35).

$$\left.\begin{aligned} Co_3O_4 + OH^- + H_2O &\rightleftharpoons 3CoOOH + e^- \\ CoOOH + OH^- &\rightleftharpoons CoO_2 + H_2O + e^- \end{aligned}\right\} \quad \text{(Eq 2)}$$

The redox peaks are more pronounced in the CV of Co_3O_4/B-rGO and indicate the charge storage in this electrode by diffusion-controlled (battery-like) process. Interestingly, the featureless (with nonzero current density) portion of the CV of Co_3O_4/B-rGO is significantly larger than that of B-rGO in both the electrolyte solutions (Fig. 3a and 4a). The presence of this featureless nature in the CV of Co_3O_4/B-rGO reveals that this electrode also stores electrochemical charge through a partial pseudocapacitive process. In addition, it is worth noting that the total area enveloped by the CV of Co_3O_4/B-rGO is much higher as compared to those by B-rGO or Co_3O_4. This indicates that the total charge stored in Co_3O_4/B-rGO is higher than that in B-rGO or Co_3O_4 (Fig. 3a and 4a). Further, a semi-quantitative estimation (not shown here) of the area of the current density versus time curves corresponding to the charging/discharging portions of CVs in all the electrodes was done. This analysis suggests that the charge obtained during charging/discharging of Co_3O_4/B-rGO is larger than that from Co_3O_4 and B-rGO together. This suggests a synergy between Co_3O_4 and B-rGO during charge storage.

The CVs from all the synthesized samples at different scan rates from 10 to 200 mV s^{-1} in 2 M KOH and 2 M NaOH are given in Figure S2 and S3, respectively. In both the electrolytes, the area enveloped by the CVs of all the samples increased with increase in the scan rate, as expected (Figure S2 and S3). The CVs of Co_3O_4 and Co_3O_4/B-rGO electrodes in Figure S2 and S3 show that the redox current increases with scan rate, predominantly because of faster ion diffusion into the electrode (Ref 21). In addition, upon increasing the scan rate, the corresponding oxidation and reduction peaks are shifted in more positive and negative potentials, respectively (Figure S2b and c and S3b and c). This is, possibly, due to an increase in the internal diffusion resistance of these electrodes with increase in scan rate (Ref 56).

For revealing the various types of charge storage natures (i.e., EDLC, pseudocapacitive and diffusion-controlled (i.e., battery-like)) in the electrodes, the relation between the peak current (i_p) and the scan rate (v), as proposed by Dunn et al. (Ref 57), is considered as shown in Eq 3 where and *a* and *b* are arbitrary parameters.

$$i_p = av^b \quad \text{(Eq 3)}$$

The value of b=1 corresponds to charge storage by EDLC; $b \approx 1$ represents pseudocapacitive nature; and b=0.5-1 indicates diffusion-controlled (i.e., battery-like) charge storage (Ref 58).

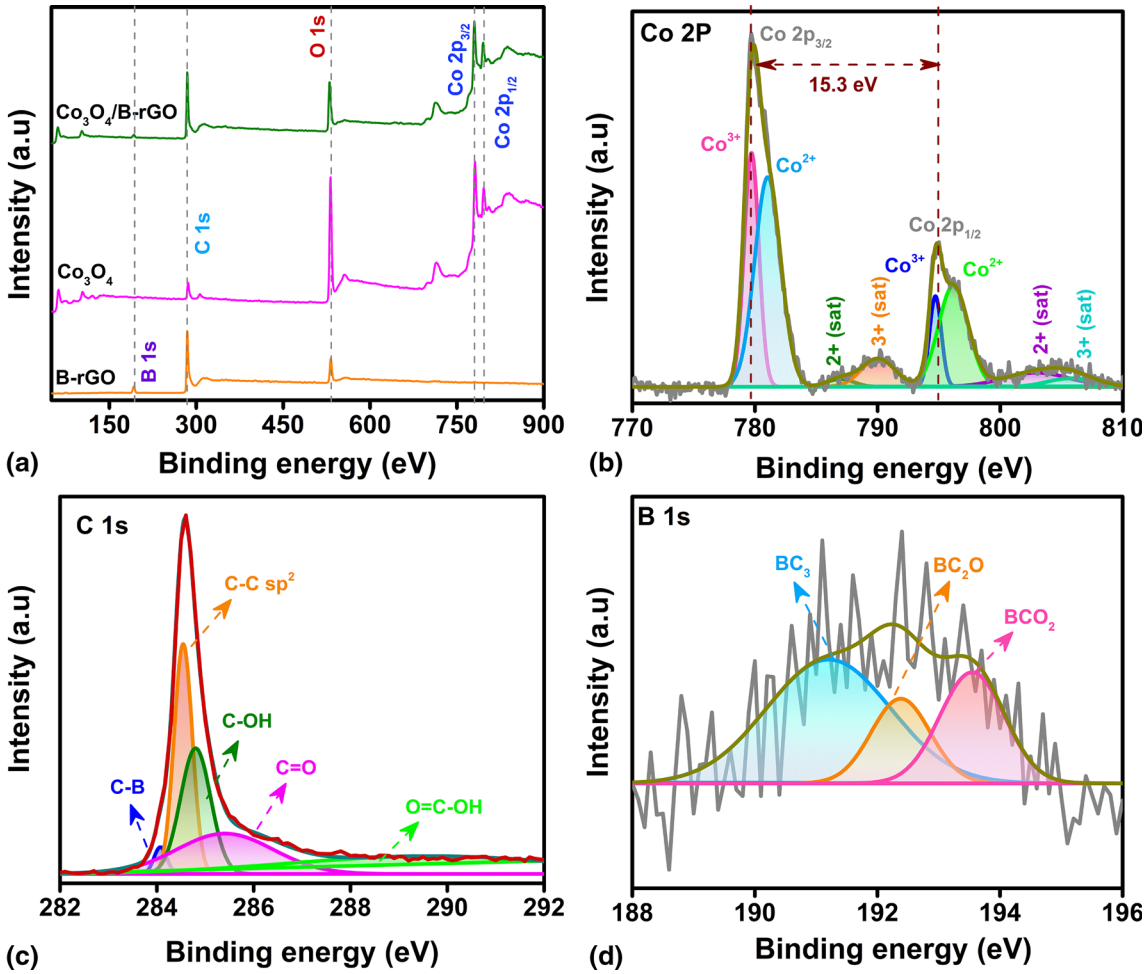

Fig. 2 (a) XPS survey spectra of B-rGO, Co_3O_4 and Co_3O_4/B-rGO. High-resolution (b) Co 2*p* (c) C 1*s* (d) B 1*s* spectra of Co_3O_4/B-rGO

Figure 3(b) and 4(b) shows that the plot between log(i_p) and log (v) is linear with the slope yielding the b values for Co_3O_4/B-rGO and Co_3O_4 in 2 M KOH and 2 M NaOH, respectively. The estimated b values are 0.80 and 0.78 for Co_3O_4/B-rGO, and 0.79 and 0.78 for Co_3O_4 in the respective electrolytes. These values of b indicate that the charge storage is taking place by diffusion-controlled (i.e., battery-like) processes.

The diffusion coefficient during charging (anodic) and discharging (cathodic) in Co_3O_4/B-rGO and Co_3O_4 is estimated by using Randles–Sevcik equation (Eq 4) (Ref 59, 60)

$$i_p = 0.4463nFAC\left(\frac{nFvD}{RT}\right)^{\frac{1}{2}} \quad \text{(Eq 4)}$$

where i_p: peak current (A), n: number of electrons per reacting species, F: Faraday's constant (96,487 C mol^{-1}), A: electrode surface area (cm^2), C: bulk electrolyte concentration (mol cm^{-3}), v: scan rate (V s^{-1}), D: diffusion coefficient (cm^2 s^{-1}), R: gas constant (8.314 J mol^{-1} K^{-1}), T: temperature (K). Figure 3(c) and 4(c) shows the log(i_p) versus log($v^{1/2}$) plots for Co_3O_4/B-rGO and Co_3O_4 in 2 M KOH and 2 M NaOH, respectively. The linear natures of these plots imply the presence of diffusion-controlled non-surface processes during charging and discharging (Ref 60). The estimated diffusion coefficients are listed in Table 1. From Table 1, the estimated D for all the electrodes in KOH is higher than those in NaOH, indicating faster ion mobility in the presence of KOH (Ref 60). This suggests that the choice of the electrolyte is vital for the improved kinetics of charge storage. Also, the D for charging/discharging of Co_3O_4/B-rGO is at least an order higher than that for either Co_3O_4 or B-rGO. This ascertains the synergy between Co_3O_4 and B-rGO during charge storage, corroborating well with the CV results (Fig. 3a and 4a). Randles–Sevcik analysis establishes that (i) B incorporated in rGO and (ii) choice of electrolyte (KOH in the present case) play vital roles in increasing the capacitance and kinetics of redox reactions.

3.2.2 Galvanostatic Charge/Discharge. The charge storage performance is further investigated by galvanostatic charge/discharge (GCD) experiments. Figure 5(a) and (b) presents the GCD curves at 0.1 A g^{-1} for all the electrodes in 2 M KOH and 2 M NaOH, respectively. Interestingly, the GCD results of B-rGO electrode (Fig. 5a and b) exhibit near-triangular charge/discharge profiles due to its EDLC nature of charge storage. The GCD results of B-rGO (Fig. 5a and b) also exhibit a partial pseudocapacitive behavior evident from the deviation from the perfect triangular shape of GCDs. Co_3O_4/B-rGO and Co_3O_4 electrodes, on the other hand, exhibit evidently nonlinear profiles in both the electrolytes due to the Faradaic diffusion-controlled processes. The area under the GCDs provides a direct evidence for the charge storage capacity of the electrode

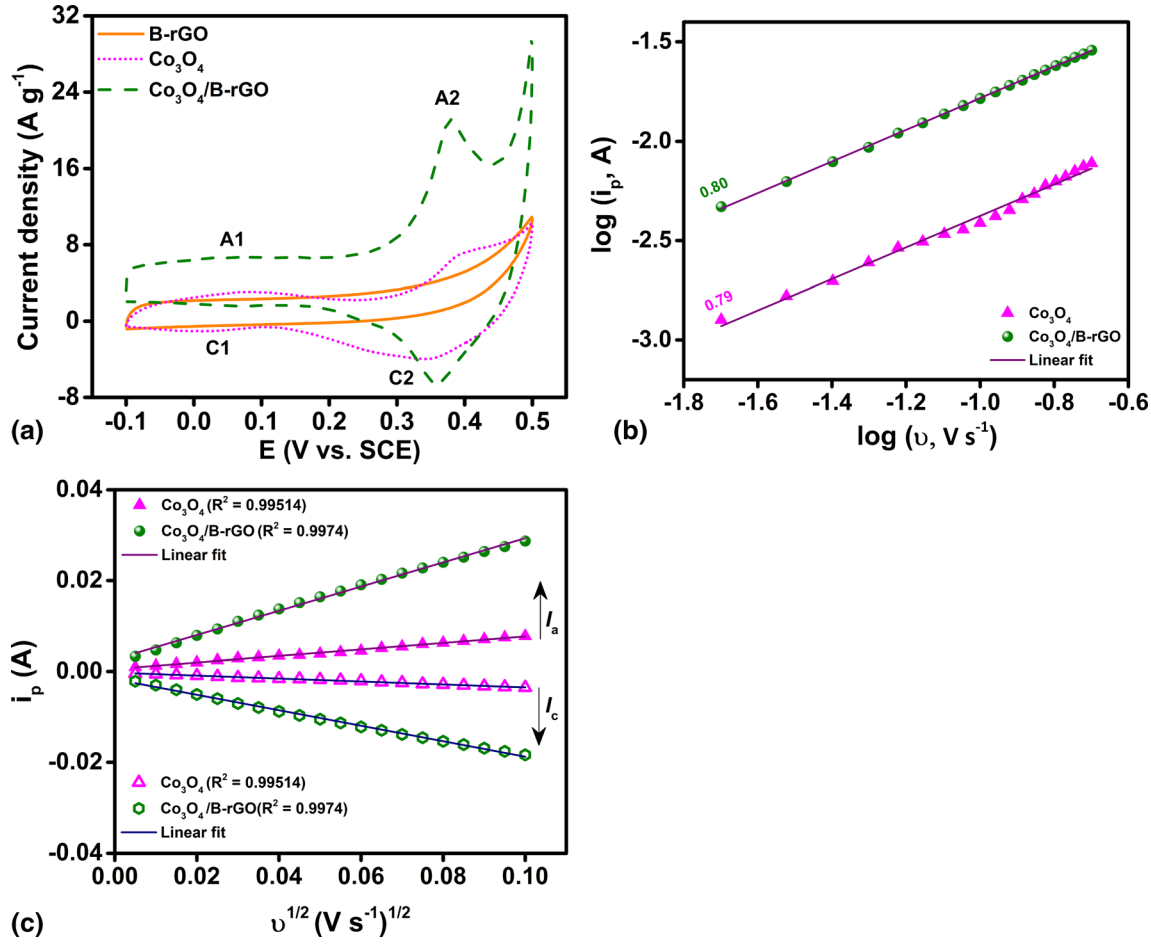

Fig. 3 (a) Cyclic voltammograms of B-rGO, Co_3O_4 and Co_3O_4/B-rGO at a scanning rate of 20 mV s^{-1} (b) log(i_p) vs. log(v) and (c) i_p vs. $v^{1/2}$ plots for Co_3O_4 and Co_3O_4/B-rGO in 2 M KOH electrolyte

material. From Fig. 5(a) and (b), this area is the highest in the Co_3O_4/B-rGO electrode signifying the relatively highest specific capacitance. This agrees well with the CVs (Fig. 3a and 4a). In Fig. 5(a) and (b), two different regions can be observed in the charging segments in Co_3O_4 containing electrodes: (i) a potential-dependent region from −0.05 V to +0.30 V versus SCE (Region I); and (ii) an almost potential independent region from +0.30 to +0.40 V versus SCE (Region II). Region I corresponds to the charge storage by electrical double-layer formation. Region II arises due to the charge storage by redox reactions involving Co^{2+} and Co^{3+} ions (i.e., diffusion-controlled and battery-like) (Ref 61). These two regions in the GCDs of the Co_3O_4/B-rGO and Co_3O_4 electrodes are in consensus with the CVs (Fig. 3a and 4a), which exhibit both the featureless nature (EDLC) and the redox peaks. Figure S4 and S5 shows that the GCD curves of all the electrodes at different current densities from 0.2 to 10.0 A g^{-1} in 2 M KOH and 2 M NaOH electrolyte solutions, respectively. These different regions are not so distinctly visible in the discharge segments as they are in the charging segments. Hence, only charging segments are discussed here. Among these GCD curves the ones in 2 M KOH possess higher areas than those in 2 M NaOH.

The specific capacity values (C_s) (C g^{-1}) of the electrodes are estimated from the GCD according to Eq 5 (Ref 62)

$$C_s = \left(\frac{I\Delta t}{m}\right) \quad \text{(Eq 5)}$$

The specific capacitance (C_{sp}) of the electrode was estimated from GCD curves using Eq 6 (Ref 63, 64)

$$C_{sp} = \left(\frac{I\Delta t}{m\Delta V}\right) \quad \text{(Eq 6)}$$

where I (A): charge/discharge current, Δt (s): time of discharge, ΔV (V): potential window and m (g): mass of the active material on the working electrode. At 0.1 A g^{-1} the estimated C_s of the B-rGO, Co_3O_4 and Co_3O_4/B-rGO electrode are 46.5, 136.6 and 270 C g^{-1}, respectively, in 2 M KOH, whereas those in 2 M NaOH are 35.4, 80.5 and 195.2 C g^{-1}, respectively. The estimated C_{sp} of all the electrodes in both 2 M KOH and 2 M NaOH are plotted in Fig. 5(c) as function of current density. From Fig. 5(c), Co_3O_4/B-rGO exhibits maximum C_{sp} of 600 (270 C g^{-1}) and 434 F g^{-1} (195 C g^{-1}) at 0.1 A g^{-1} in 2 M KOH and 2 M NaOH, respectively. This is consistent with the largest area enclosed by the CVs of this electrode (Fig. 3a and 4a). At the highest current density tested (i.e. 10 A g^{-1}, Fig. 5c), the C_{sp} of Co_3O_4/B-rGO drops to 454 F g^{-1} (204 C g^{-1}) and 313 F g^{-1} (141 C g^{-1}) in 2 M KOH and 2 M NaOH, respectively, still being the highest among all the electrodes. The drop in specific

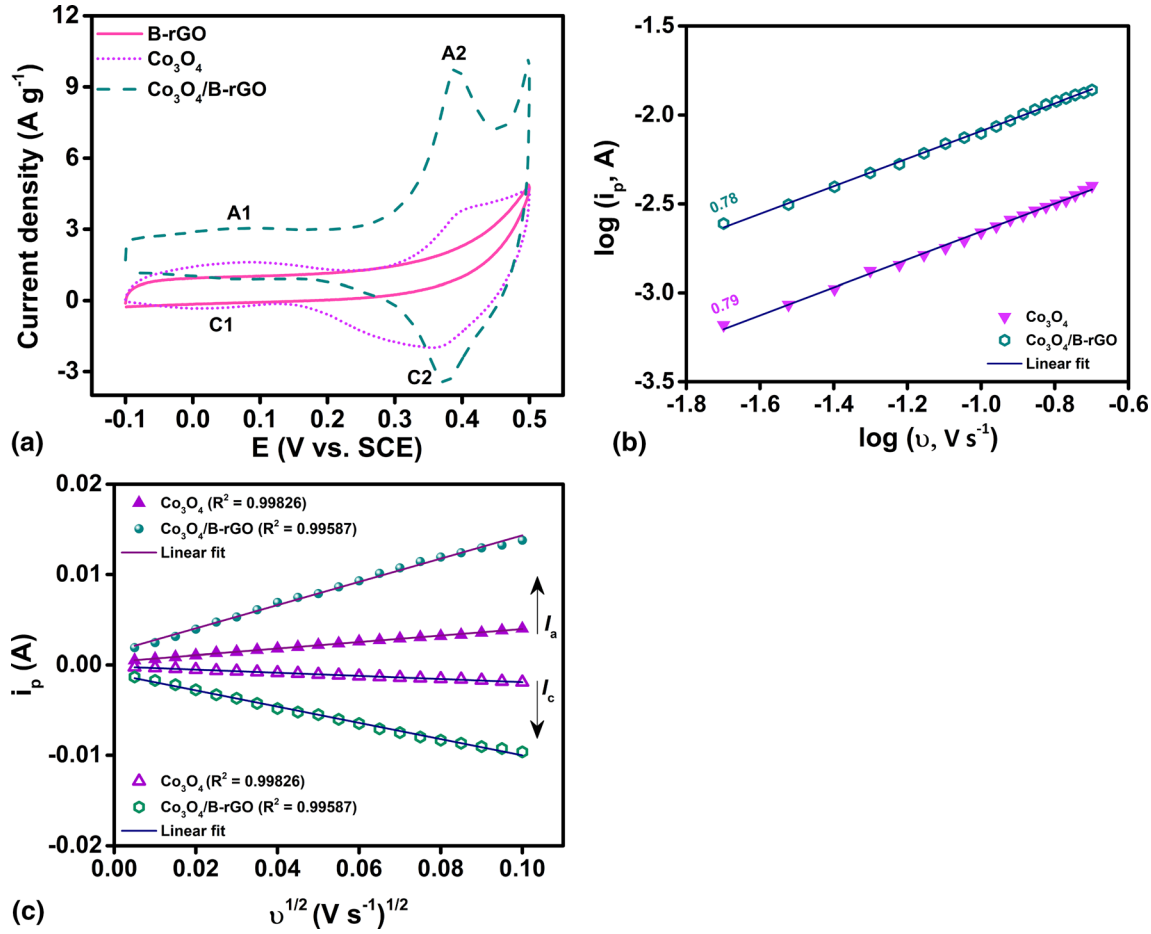

Fig. 4 (a) Cyclic voltammograms of B-rGO, Co_3O_4 and Co_3O_4/B-rGO at a scanning rate of 20 mV s^{-1} (b) log(i_p) vs. log(v) and (c) i_p vs. $v^{1/2}$ plots for Co_3O_4 and Co_3O_4/B-rGO in 2 M NaOH electrolyte

capacitance with increase in current density can be explained as follows. At lower current densities, there is sufficient time for interaction between Co_3O_4/B-rGO electrode and electrolyte ions, allowing the storage of a large amount of charge in the electrode leading to high specific capacitance. With increase in the current density, this interaction time decreases and fast kinetics of the Faradaic reaction leading to only partial charge storage and lower specific capacitance (Ref 56).

The enhanced specific capacitance in the Co_3O_4/B-rGO electrode is due to (i) the presence of B in rGO network; (ii) the combination of Co_3O_4 (diffusion-controlled) in B-rGO (EDLC and pseudocapacitance); and (iii) the choice of 2 M KOH electrolyte.

The specific capacitance values of the Co_3O_4/B-rGO in the present study are compared with those reported for various Co_3O_4-graphene-based materials at various current densities from literature and summarized in Table 2. The present C_{sp} values of Co_3O_4/B-rGO are either superior by 95 to 823% or inferior only by 18 to 50% as compared to the values reported in literature. At the highest current density tested (i.e., 10 A g^{-1}), the present Co_3O_4/B-rGO-KOH system exhibits a C_{sp} of 454 F g^{-1} (204 C g^{-1}), which is higher by a remarkable 224% compared to Co_3O_4/rGO-6 M KOH (140 F g^{-1} (Ref 65)). However, it is lower by only 50% compared to Co_3O_4/rGO-2 M KOH (916.5 F g^{-1} (Ref 35)) (see Table 2). A close observation of these two systems shows that the Co_3O_4/rGO-2 M KOH is synthesized by laser irradiation (Ref 35), whereas the present Co_3O_4/rGO is synthesized by a combination of electrochemical exfoliation (for rGO) and hydrothermal route for B incorporation and Co_3O_4 loading. This clearly shows that apart from the active material–electrolyte combination, the synthesis method also plays a vital role in enhancing the charge storage. Interestingly, this suggests that the present synthesis method is viable with several other synthesis methods reported in literature (at various other current densities).

To study the cyclic stability of all the electrodes of the present study, C_{sp} is plotted as function of number of cycles (Fig. 5d) and the cyclability curves are plotted after every 200 cycles (Figure S6 and S7) for 2 M KOH and 2 M NaOH cases. From Fig. 5(d), S6 and S7, the Co_3O_4/B-rGO-KOH system exhibits the best capacitance retention of 87.8% after 2000 cycles.

The Coulombic efficiency of the synthesized electrodes is calculated using Eq 7

$$\eta = \frac{\Delta t_d}{\Delta t_c} \times 100\% \qquad \text{(Eq 7)}$$

where η: Coulombic efficiency Δt_d: discharging time and Δt_c: charging time. Figure 5(e) shows the Coulombic efficiency of the electrodes in 2 M KOH and 2 M NaOH electrolytes. After 2000 cycles, the ηs of B-rGO, Co_3O_4 and Co_3O_4/B-rGO electrodes are 94, 98 and 97% respectively, in 2 M

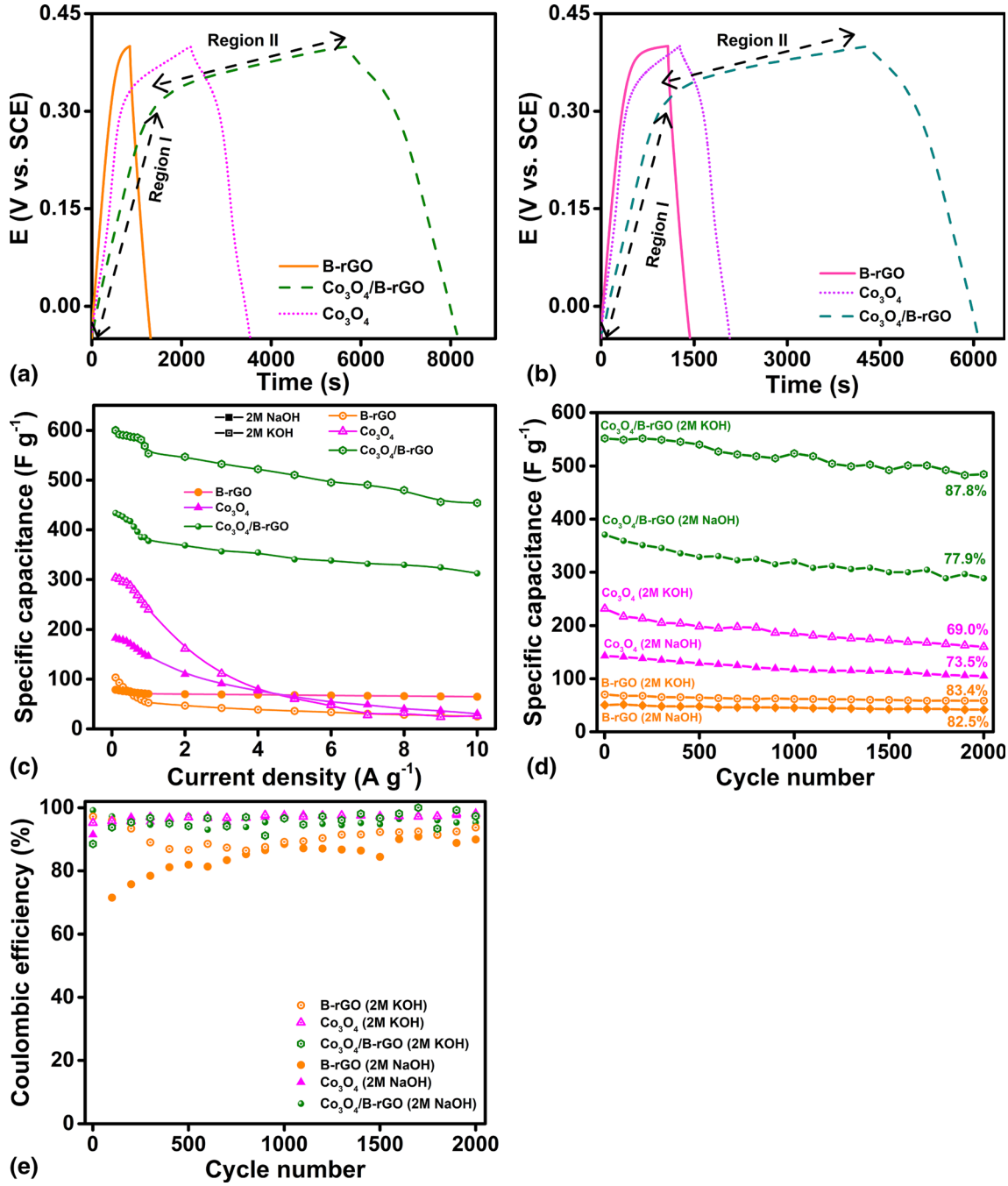

Fig. 5 GCD curves of B-rGO, Co_3O_4 and Co_3O_4/B-rGO at 0.1 Ag^{-1} in (a) 2 M KOH (b) 2 M NaOH (c) Specific capacitance at different current densities (d) Capacitance retention at 1 A g^{-1} (e) Coulombic efficiency of B-rGO, Co_3O_4 and Co_3O_4/B-rGO in 2 M KOH and 2 M NaOH electrolyte

KOH; they are 90, 98 and 95% respectively, in 2 M NaOH. This suggests that the 2 M KOH offers better Coulombic efficiency and excellent kinetic reversibility than 2 M NaOH.

3.2.3 Electrochemical Impedance Spectroscopy. Electrochemical impedance spectroscopy (EIS) was performed to, further, understand the charge storage kinetics, estimate the solution and charge transfer resistances, and the charge storage mechanism. EIS results of the B-rGO, Co_3O_4 and Co_3O_4/B-rGO electrodes in the case of 2 M KOH and 2 M NaOH are shown in Fig. 6 and 7, respectively. Figure 6(a) and 7(a) shows the Nyquist plots for all the electrodes in 2 M KOH and 2 M NaOH, respectively. The insets in these figures show the magnified view of the high-frequency regions. The Bode plots of phase angle versus frequency (ϕ versus log(f)) and impedance versus frequency (log|z| versus log(f)) are also shown in Fig. 6(b) and 7(b), and Fig. 6(c) and 7(c), respectively. The shapes of the Bode plots are similar to those reported in literature (Ref 66). The obtained Nyquist plots for all the electrodes were fitted with the equivalent circuit shown within Fig. 6(a) and 7(a) using ZSimpWin 3.21 software. The values of the various optimized parameters obtained after fitting are listed in Table S1 and Table S3 for 2 M KOH and 2 M

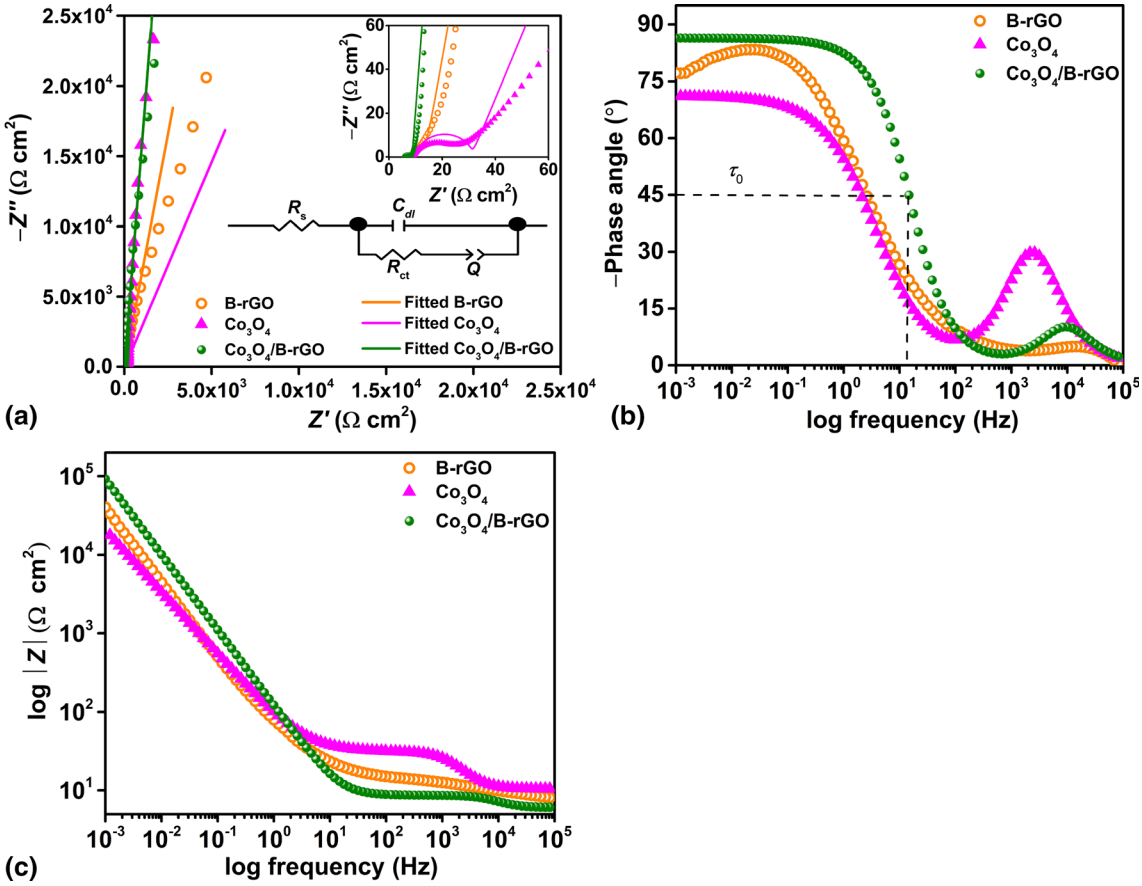

Fig. 6 EIS data of the B-rGO, Co_3O_4 and Co_3O_4/B-rGO in 2 M KOH (a) Nyquist plot (insets: enlarged high-frequency region and equivalent circuit) (b) Bode plot of phase angle vs. frequency and (c) Bode plot of impedance vs. frequency

NaOH, respectively. The intercept in the real axis at the highest frequency in the Nyquist plot represents the electrolyte solution resistance (R_s). The estimated R_s of Co_3O_4/B-rGO in 2 M KOH and 2 M NaOH electrolytes are 6.08 and 6.72 Ω cm^2, respectively. Interestingly, these R_s values, corresponding to Co_3O_4/B-rGO, are the smallest among those for all the electrodes in both 2 M KOH (Table S1) and 2 M NaOH cases (Table S2). Further, the R_s value for Co_3O_4/B-rGO in 2 M KOH is smaller than that in 2 M NaOH. This clearly shows the advantage of using KOH (i.e., K^+ ions) over NaOH (i.e., Na^+ ions). The semicircle at high-frequency region is fitted to a charge transfer resistance (R_{ct}), involving the exchange of OH^- ions (Ref 67). The obtained values for Co_3O_4/B-rGO are 2.61 and 3.76 Ω cm^2, in 2 M KOH and 2 M NaOH electrolytes, respectively. These values for the Co_3O_4 electrode are 20.69 and 30.49 Ω cm^2. Thus, interestingly, the presence of B-rGO causes a remarkable one order drop in R_{ct} and accelerated the redox reactions (Eq 2). This remarkable drop in R_{ct} is attributed to the electron deficient nature of the B-rGO aiding in accelerating the OH^- exchange (Ref 68). This corroborates well with the highest estimated values of the diffusion coefficient in Co_3O_4/B-rGO, as reported in Fig. 3(c) and 4(c). Moreover, the smaller R_{ct} in the case of 2 M KOH compared to that in the case of 2 M NaOH is worth noticing. Most likely, the relatively low hydration sphere radius of K^+ (3.31 Å) compared with that of Na^+ (3.58 Å) is the reason for this improvement in R_{ct} (Ref 68). These results show that the charge transfer process of electrode also depends upon the size of cation present in the electrolyte.

In order to understand the extent of capacitive nature of these electrodes, a constant phase element (CPE, denoted as Q in Fig. 6 and 7) is used in modeling the equivalent circuit. Q is given by Eq 8

$$Q = Y_0 B(j\omega)^n \quad \text{(Eq 8)}$$

where B and n ($0<n<1$): frequency-independent parameters, Yo: admittance. When $n=1$, the electrochemical system behaves as a pure capacitor; and when $n=0$, it behaves as a pure resistor (Ref 69). The estimated n values of B-rGO are the highest (0.8952 for 2 M KOH; 0.8947 for 2 M NaOH) among all the electrodes tested. This indicates that B-rGO has the highest capacitive nature. The estimated n values of Co_3O_4/B-rGO (0.80 in both 2 M KOH and 2 M NaOH) are lower than those of B-rGO. This is, mainly, due to the increased diffusion-controlled (i.e., battery-like) nature upon anchoring Co_3O_4 on to B-rGO. This diffusion-controlled redox reactions offer electrochemical resistance, leading to a decrease in the n value. Interestingly, the estimated n values for Co_3O_4/B-rGO are higher than those for bare Co_3O_4 electrode (0.7907 for 2 M KOH; 0.7962 for 2 M NaOH). This increase in the capacitive nature of Co_3O_4/B-rGO is attributed to the addition of B-rGO to Co_3O_4. That is, B-rGO imparts some capacitive nature to Co_3O_4/B-rGO.

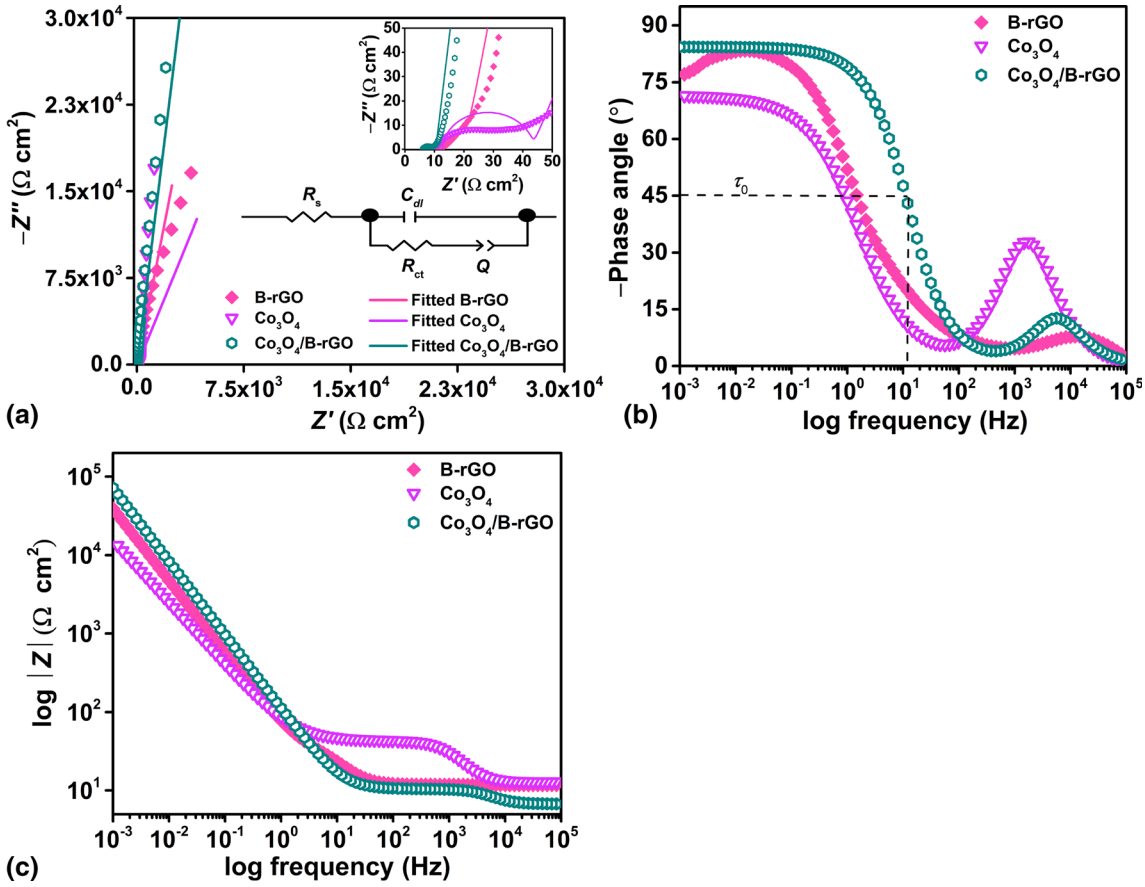

Fig. 7 EIS data of the B-rGO, Co_3O_4 and Co_3O_4/B-rGO in 2 M NaOH (a) Nyquist plot (insets: enlarged high-frequency region and equivalent circuit) (b) Bode plot of phase angle vs. frequency and (c) Bode plot of impedance vs. frequency

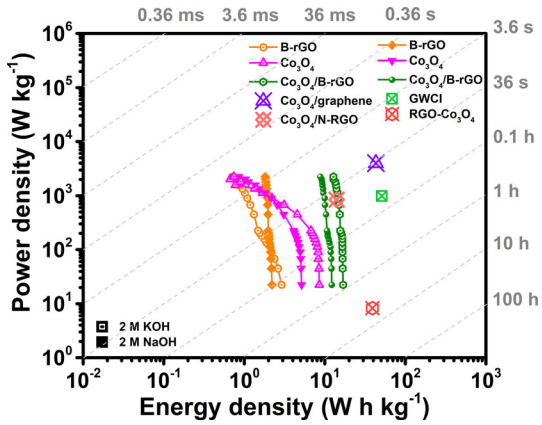

Fig. 8 Ragone plots of the prepared B-rGO, Co_3O_4, and Co_3O_4/B-rGO electrodes in 2 M KOH and NaOH electrolytes and different reported studies (Such as GWCI (Ref 74), RGO-Co_3O_4 (Ref 71), Co_3O_4/graphene (Ref 35) and Co_3O_4/N-RGO (Ref 56))

To estimate the relaxation time (τ_o) and to further ascertain the charge storage nature, the Bode plots of phase angle versus frequency for all the electrodes in 2 M KOH (Fig. 6b) and 2 M NaOH (Fig. 7b) are used (Ref 20). The estimated relaxation times ($\tau_o = 1/f_0$; where f_0: frequency at a phase angle of 45°) (Ref 70) are reported in Table S2 for 2 M KOH and Table S4 for 2 M NaOH. The order of the estimated τ_o is B-rGO>Co_3O_4 >Co_3O_4/B-rGO for both the electrolyte systems. The Co_3O_4/B-rGO electrode exhibits the least relaxation time of 0.067 and 0.089 s for the cases of 2 M KOH and 2 M NaOH, respectively. The τ_o of the present Co_3O_4/B-rGO is at least 200 times smaller than those reported in literature for the similar material (20 s) (Ref 71), and thus suggesting that the present Co_3O_4/B-rGO superior. The lowest τ_o of Co_3O_4/B-rGO suggests that it exhibits the best frequency response and rate performances as evidenced from CV analysis (Fig. 3 and 4) and the GCD results (Fig. 5). Moreover, the lower τ_o of Co_3O_4/B-rGO in the 2 M KOH case compared with the 2 M NaOH case reiterates that the Co_3O_4/B-rGO-KOH electrode–electrolyte combination demonstrates the best performance among the tested electrodes and electrolytes. Interestingly, the frequency response and the rate performance of B-rGO is less than that of Co_3O_4, possibly, because of the *p*-doping effect in the former electrode needing longer times. Further, anchoring Co_3O_4 to B-rGO reduces the τ_o of the former (Table S2 and S4), indicating enhanced frequency response and the rate performance of the obtained composite electrodes. This enhanced behavior is due to the strong interaction between Co_3O_4 and B-rGO (Fig. 2).

The phase angles of 86° and 84° for Co_3O_4/B-rGO nanocomposite electrode in 2 M KOH and 2 M NaOH electrolytes at low frequencies (Fig. 6b and 7b) reinforce the capacitive charge storage nature of these electrodes (Ref 72). However, both these values are slightly lower than that for an ideal capacitor (90°). The phase angle values suggest that the Co_3O_4/B-rGO electrode enjoys the benefits of both (i) the

Table 1 Diffusion coefficient (*D*) values of the synthesized electrodes

Electrode materials	Electrolyte	Diffusion coefficient, *D*, $cm^2\ s^{-1}$	
		Charging	Discharging
Co_3O_4	2 M KOH	1.81×10^{-5}	3.75×10^{-6}
	2 M NaOH	4.61×10^{-6}	1.07×10^{-6}
Co_3O_4/B-rGO	2 M KOH	2.53×10^{-4}	1.04×10^{-4}
	2 M NaOH	5.92×10^{-5}	2.89×10^{-5}

Table 2 Summary of the electrochemical performance of Co_3O_4/B-rGO electrodes of the present study compared with the previous reports on Co_3O_4/rGO based electrode systems in the three-electrode assembly

Current density, A g^{-1}	Electrode materials	Preparation method	Electrolyte	Specific capacitance, F g^{-1}	References
0.1	Co_3O_4/B-rGO	Hydrothermal	2 M KOH	600	This work
	Co_3O_4/B-rGO	Hydrothermal	2 M NaOH	434	This work
	Co_3O_4/Graphene	Hydrothermal	2 M KOH	157.7	38
0.2	Co_3O_4/B-rGO	Hydrothermal	2 M KOH	592	This work
	Co_3O_4/B-rGO	Hydrothermal	2 M NaOH	430	This work
	rGO-Co_3O_4	Hydrothermal	1 M KOH	278	79
0.5	Co_3O_4/B-rGO	Hydrothermal	2 M KOH	588	This work
	Co_3O_4/rGO	Hydrothermal	6 M KOH	545	80
	Co_3O_4/B-rGO	Hydrothermal	2 M NaOH	418	This work
	Co_3O_4/rGONS	Hydrothermal	1 M KOH	445	81
	Co_3O_4/rGO	Electrochemical	2 M NaOH	357	82
	rGO-Co_3O_4	Hydrothermal	1 M KOH	123	79
1	Co_3O_4/graphene	Laser irradiation	2 M KOH	978.1	35
	Co_3O_4 @RGO	Hydrothermal	6 M KOH	894	83
	Co_3O_4/RGO	Chemical route	3.5 M KOH	784	21
	GWCI	Microwave irradiation	0.5 M BMIM-BF_4/CH_3CN	712	74
	Co_3O_4/CNFs	Electrospinning	6 M KOH	586	34
	Co_3O_4/B-rGO	Hydrothermal	2 M KOH	554	This work
	Co_3O_4/NGF	Chemical vapor deposition	1 M KOH	451	84
	Co_3O_4 @GE	Hydrothermal	6 M KOH	430	39
	Co_3O_4/graphene	Liquid-phase exfoliation	6 M KOH	392	85
	Co_3O_4/B-rGO	Hydrothermal	2 M NaOH	378	This work
	rGO/Co_3O_4	Chemical route	6 M KOH	291	86
	Co_3O_4/rGO	Two-step surfactant-assisted	6 M KOH	163.8	65
	Co_3O_4/Graphene	Hydrothermal	2 M KOH	60	38
3	Co_3O_4/B-rGO	Hydrothermal	2 M KOH	532	This work
	Co_3O_4/rGO	Electrochemical	2 M NaOH	256	82
5	Co_3O_4/B-rGO	Hydrothermal	2 M KOH	511	This work
	Graphene/Co_3O_4	Hydrothermal	6 M KOH	443	87
	Co_3O_4/RGO	Chemical route	3.5 M KOH	432	21
	Co_3O_4/B-rGO	Hydrothermal	2 M NaOH	341	This work
	RGO/Co_3O_4	Nanosheet assembly	6 M KOH	331	88
	Co_3O_4/rGONS	Hydrothermal	1 M KOH	262	81
7	GWCI	Microwave irradiation	0.5 M BMIM-BF_4/CH_3CN	600	74
	Co_3O_4/B-rGO	Hydrothermal	2 M KOH	491	This work
	Co_3O_4/B-rGO	Hydrothermal	2 M NaOH	332	This work
8	Co_3O_4/B-rGO	Hydrothermal	2 M KOH	480	This work
	Co_3O_4/B-rGO	Hydrothermal	2 M NaOH	330	This work
	rGO/Co_3O_4	Chemical route	6 M KOH	232	86
10	Co_3O_4/graphene	Laser irradiation	2 M KOH	916.5	35
	Co_3O_4/B-rGO	Hydrothermal	2 M KOH	454	This work
	Co_3O_4 @GE	Hydrothermal	6 M KOH	320	39
	Co_3O_4/graphene	Liquid-phase exfoliation	6 M KOH	392	85
	Co_3O_4/B-rGO	Hydrothermal	2 M NaOH	313	This work
	Co_3O_4/rGO	Two-step surfactant-assisted	6 M KOH	140	65

diffusion-controlled and higher charge storage from Co_3O_4 (Fig. 3a and 4a) coupled with (ii) the charge storage stability of B-rGO (Fig. 5c and 5d). A close observation of Fig. 6(b) and 7 (b) shows the existence of a broad peak in the high-frequency region for the Co_3O_4 containing electrode, which is related to the diffusive resistance of the electrode (Ref 66). In the case of Co_3O_4/B-rGO, this peak appears at the highest frequencies. The similar peak in the case of Co_3O_4 appears at lower frequencies, compared with that in Co_3O_4/B-rGO (Fig. 6b and 7b). The presence of the peak at the highest frequencies among all the electrodes suggests that the Co_3O_4/B-rGO exhibits lowest diffusive resistance (Ref 66). Further, the peak frequency values for the Co_3O_4/B-rGO electrode in 2 M KOH and 2 M NaOH electrolytes are 10,056 and 5680 Hz respectively. This clearly indicates that the diffusive resistance decreases further when 2 M KOH is employed as the electrolyte. This also indicates that the K^+ are easily accessible compared to the Na^+ (Ref 73),

rendering the performance improvement of Co_3O_4/B-rGO electrode when employed with 2 M KOH electrolyte.

3.2.4 Energy and Power Density. The energy and power densities, which indicate the performance of the supercapacitors for practical applications, were calculated from the GCD curves using Eq 9. These energy and power densities are shown as Ragone plots in Fig. 8 for all the electrodes in both 2 M KOH and 2 M NaOH electrolytes.

$$\left.\begin{aligned} E &= \left(\frac{1}{2} C_{sp} V^2\right) \\ P &= \left(\frac{E}{\Delta t}\right) \end{aligned}\right\} \qquad \text{(Eq 9)}$$

where V: potential range (V), Δt: discharge time (h), E: energy density (W h kg^{-1}) and P: power density (W kg^{-1}). Figure 8 shows the values reported in literature for similar setup configuration (i.e., three-electrode configuration) electrodes such as graphene-wrapped and cobalt oxide-intercalated (GWCI) (Ref 74), RGO-Co_3O_4 (Ref 71), Co_3O_4/graphene (Ref 35) and Co_3O_4/N-RGO (Ref 56). As expected, the energy density decreases and power density increases on increasing the current density from 0.1 to 10 A g^{-1}. It can be observed that the energy density of all the electrodes is higher in 2 M KOH as compared with those in 2 M NaOH. The Co_3O_4/B-rGO nanocomposite electrode exhibits the highest energy densities of 16.87 W h kg^{-1} in 2 M KOH and 12.20 W h kg^{-1} in 2 NaOH. Co_3O_4/B-rGO-KOH system yields a maximum power density of 2250 W kg^{-1} with an energy density of 12.77 W h kg^{-1} at the highest current density of 10 A g^{-1}. This is better than the power density values reported in literature for similar materials. For example, a Co_3O_4/graphene-based electrode resulted in 986.32 W kg^{-1} (50.96 W h kg^{-1}) (Ref 74). The RGO-Co_3O_4 electrode prepared by Xiang et al. (Ref 71) exhibited 8.3 W kg^{-1} (39 W h kg^{-1}). The Co_3O_4/N-RGO electrode prepared by Tian et al. (Ref 56) yielded 843 W kg^{-1} (14 W h kg^{-1}). Among the electrodes in the present study, the B-rGO electrode delivered the lowest energy density of 2.91 W h kg^{-1} (in 2 M KOH) and 2.21 W h kg^{-1} (in 2 NaOH), as a result of its EDLC nature. The Ragone plot (Fig. 8) suggests that the present Co_3O_4/B-rGO-KOH system is suitable for high power and high energy applications.

From the results of electrochemical experiments presented in Fig. 3, 4, 5, 6, 7, and 8 from 2 M KOH and 2 M NaOH, the results within KOH are more promising for supercapacitor applications. For example, the CVs at all the scan rates (Fig. 3a, 4a, S2 and S3) and GCDs (Fig. 5a, b, S4 and S5) show that the enclosed areas, and thus, the charge storage, for all the electrodes in 2 M KOH case, is higher than their counterparts in 2 M NaOH case. Further, from EIS analysis (Table S1 and S3), 2 M KOH electrolyte offers a smaller solution and charge transfer resistances than 2 M NaOH. Also, the relaxation times are lower in the case of 2 M KOH (Table S2 and S4). The enhanced electrochemical behavior of all the electrodes in 2 M KOH is responsible for the higher energy storage in this electrolyte as seen from Ragone plot (Fig. 8). The benefits of using 2 M KOH are due to the high ionic mobility (7.6×10^{-5} cm^2 s^{-1} v^{-1}) and molar conductivity (73.5 cm^2 Ω^{-1} mol^{-1}) of K^+ than those of Na^+ (5.2×10^{-5} cm^2 s^{-1} v^{-1}; 50. 1 cm^2 Ω^{-1} mol^{-1}) in aqueous solutions (Ref 75, 76). This higher ionic mobility and molar conductivity of K^+ is due to the weaker interaction of K^+ with water molecules (Ref 73, 75-77). Moreover, K^+ has low hydration sphere radius (3.31 Å) than Na^+ ion (3.58 Å) due to the strong $Na^{\delta+}$–$H_2O^{\delta-}$ interaction (Ref 78). Further, the hydration number is also important criteria for deciding the charge storage capability. K^+ ion has low hydration number (7) than Na^+ (13) ions (Ref 78). This means that K^+ ion can release water molecules more easily than Na^+ during charge storage, leading to the improved specific capacitance of the electrodes. In contrast, Na^+ ions exhibit difficulty in moving through the electrolyte compared to K^+ ions. Hence, the device exhibits higher charger storage in 2 M KOH electrolyte.

It can be concluded from the present study that the combination of the electrode and electrolyte decides the overall performance. Among the set of electrodes and electrolytes used, Co_3O_4/B-rGO composite electrode in 2 M KOH yields the best electrochemical performance and the highest energy density at a given power density. Hence, it can be employed in the applications requiring high power and high energy densities.

4. Conclusions

The electrochemical behavior of hydrothermally synthesized B incorporated reduced graphene oxide (B-rGO) (where rGO is synthesized by electrochemical exfoliation); Co_3O_4; and Co_3O_4 anchored to B-rGO (Co_3O_4/B-rGO) are studied in 2 M KOH and NaOH electrolytes for supercapacitor applications. The purity and chemical nature of these materials was confirmed by x-ray diffraction (XRD) and x-ray photoelectron spectroscopy (XPS). During cyclic voltammetry, the B-rGO electrode exhibits a featureless shape, which indicates partial electrical double-layer capacitance (EDLC) and pseudocapacitance. On the other hand, Co_3O_4 shows two reversible redox peaks suggesting diffusion-controlled (i.e., battery-like) processes for the formation of CoOOH and CoO_2 upon OH^- insertion. Interestingly, the Co_3O_4/B-rGO nanocomposite electrode shows both pseudocapacitive and battery-like behavior. The charge storage behaviors of all the electrodes are investigated through galvanostatic charge/discharge (GCD) experiments and electrochemical impedance spectroscopy (EIS). Interestingly, the specific capacitance (C_{sp}) estimated from GCD is higher in all the electrodes in 2 M KOH than in 2 M NaOH. The Co_3O_4/B-rGO in 2 M KOH shows the highest C_{sp} of 600 F g^{-1} (270 C g^{-1}) at 0.1 A g^{-1} and 454 F g^{-1} (204 C g^{-1}) at 10 A g^{-1}. At 1 A g^{-1} the capacitance retention in the Co_3O_4/B-rGO-KOH system is 87.8%, demonstrating very good cyclic stability up to 2000 cycles, despite being partially diffusion-controlled in nature. The Co_3O_4/B-rGO-KOH system yields maximum power density of 2250 W kg^{-1} with an energy density of 8.79 W h kg^{-1} at 10 A g^{-1}. The superior performance in KOH over NaOH is attributed to the low hydration sphere radius, high ionic conductivity, and the estimated low diffusive and charge transfer resistance, indicating good ionic accessibility of K^+ into electrode. The present study shows that the combination of the electrode and electrolyte decides the overall performance for supercapacitor applications.

Acknowledgments

Support from Industrial Research & Consultancy Centre, Indian Institute of Technology Bombay, India (Grant No. RI/0316-

10001239-001) and Indian Space Research Organisation (ISRO/STC/IITB/2019-20/Dt. 10/10/2019, Grant: 10013762) is greatly appreciated.

References

1. J. Chmiola, C. Largeot, P.-L. Taberna, P. Simon, and Y. Gogotsi, Monolithic Carbide-Derived Carbon Films for Micro-supercapacitors, *Science*, 2010, **328**(5977), p 480–483
2. L.L. Zhang and X.S. Zhao, Carbon-Based Materials as Supercapacitor Electrodes, *Chem. Soc. Rev.*, 2009, **38**(9), p 2520–2531
3. R. Ramachandran, C. Zhao, D. Luo, K. Wang, and F. Wang, Synthesis of Copper Benzene-1, 3, 5-Tricarboxylate Metal Organic Frameworks with Mixed Phases as the Electrode Material for Supercapacitor Applications, *Appl. Surf. Sci.*, 2018, **460**, p 33–39
4. C. Singh and A. Paul, Physisorbed Hydroquinone on Activated Charcoal as a Supercapacitor: An Application of Proton-Coupled Electron Transfer, *J. Phys. Chem. C*, 2015, **119**(21), p 11382–11390
5. Q. Ke, Y. Liu, H. Liu, Y. Zhang, Y. Hu, and J. Wang, Surfactant-Modified Chemically Reduced Graphene Oxide for Electrochemical Supercapacitors, *RSC Adv.*, 2014, **4**(50), p 26398–26406
6. K. Wang, C. Li, and B. Ji, Preparation of Electrode Based on Plasma Modification and Its Electrochemical Application, *J. Mater. Eng. Perform.*, 2014, **23**(2), p 588–592
7. O. Pech and S. Maensiri, Effect of Calcining Temperature on Electrospun Carbon Nanofibers for Supercapacitor, *J. Mater. Eng. Perform.*, 2020, **29**(4), p 2386–2394
8. A.K. Geim and K.S. Novoselov, The rise of graphene, *Nat. Mater.*, 2007, **6**, p 183–191
9. C. Zhang, Y. Huang, S. Tang, M. Deng, and Y. Du, High-Energy All-Solid-State Symmetric Supercapacitor Based on Ni_3S_2 Mesoporous Nanosheet-Decorated Three-Dimensional Reduced Graphene Oxide, *ACS Energy Lett.*, 2017, **2**(4), p 759–768
10. N.E. Tran, S.G. Lambrakos, and J.J. Lagowski, Analysis of Capacitance Characteristics of C60, C70, and La@C82, *J. Mater. Eng. Perform.*, 2009, **18**(1), p 95–101
11. H. Pal, S. Bhubna, P. Kumar, R. Mahapatra, and S. Chatterjee, Synthesis of Flexible Graphene/Polymer Composites for Supercapacitor Applications, *J. Mater. Eng. Perform.*, 2018, **27**(6), p 2668–2672
12. K.P. Gannavarapu, S. Azizighannad, M. Molli, M. Pandey, S. Muthukumar, S. Mitra, and R.B. Dandamudi, Nanoporous Hierarchical Carbon Structures Derived from Fungal Basidiocarps for High Performance Supercapacitors, *Energy Storage*, 2019, **1**(3), p e58
13. G. Wang, L. Zhang, and J. Zhang, A Review of Electrode Materials for Electrochemical Supercapacitors, *Chem. Soc. Rev.*, 2012, **41**(2), p 797–828
14. Y. Wang, Y. Song, and Y. Xia, Electrochemical Capacitors: Mechanism, Materials, Systems, Characterization and Applications, *Chem. Soc. Rev.*, 2016, **45**(21), p 5925–5950
15. Z. Wen, X. Wang, S. Mao, Z. Bo, H. Kim, S. Cui, G. Lu, X. Feng, and J. Chen, Crumpled Nitrogen-Doped Graphene Nanosheets with Ultrahigh Pore Volume for High-Performance Supercapacitor, *Adv. Mater.*, 2012, **24**(41), p 5610–5616
16. J. Han, L.L. Zhang, S. Lee, J. Oh, K.-S. Lee, J.R. Potts, J. Ji, X. Zhao, R.S. Ruoff, and S. Park, Generation of B-Doped Graphene Nanoplatelets Using a Solution Process and Their Supercapacitor Applications, *ACS Nano*, 2013, **7**(1), p 19–26
17. S. Li, Z. Wang, H. Jiang, L. Zhang, J. Ren, M. Zheng, L. Dong, and L. Sun, Plasma-Induced Highly Efficient Synthesis of Boron Doped Reduced Graphene Oxide for Supercapacitors, *Chem. Commun.*, 2016, **52**(73), p 10988–10991
18. X.A. Chen, X. Chen, X. Xu, Z. Yang, Z. Liu, L. Zhang, X. Xu, Y. Chen, and S. Huang, Sulfur-Doped Porous Reduced Graphene Oxide Hollow Nanosphere Frameworks as Metal-Free Electrocatalysts for Oxygen Reduction Reaction and as Supercapacitor Electrode Materials, *Nanoscale*, 2014, **6**(22), p 13740–13747
19. Y. Wen, B. Wang, C. Huang, L. Wang, and D. Hulicova-Jurcakova, Synthesis of Phosphorus-Doped Graphene and its Wide Potential Window in Aqueous Supercapacitors, *Chem. Eur. J.*, 2015, **21**(1), p 80–85
20. R.N. Muthu and S.S.V. Tatiparti, Electrode and Symmetric Supercapacitor Device Performance of Boron-Incorporated Reduced Graphene Oxide Synthesized By Electrochemical Exfoliation, *Energy Storage*, 2020, **2**(4), p e134
21. K. Subramani, S. Kowsik, and M. Sathish, Facile and Scalable Ultrafine Cobalt Oxide/Reduced Graphene Oxide Nanocomposites for High Energy Asymmetric Supercapacitors, *ChemistrySelect*, 2016, **1**(13), p 3455–3467
22. G.-S. Jang, S. Ameen, M.S. Akhtar, E. Kim, and H.-S. Shin, Electrochemical Investigations of Hydrothermally Synthesized Porous Cobalt Oxide (Co_3O_4) Nanorods: Supercapacitor Application, *ChemistrySelect*, 2017, **2**(28), p 8941–8949
23. X. Wang, H. Xia, X. Wang, J. Gao, B. Shi, and Y. Fang, Facile Synthesis Ultrathin Mesoporous Co_3O_4 Nanosheets for High-Energy Asymmetric Supercapacitor, *J. Alloys Compd.*, 2016, **686**, p 969–975
24. C.V. Niveditha, R. Aswini, M.J. Jabeen Fatima, R. Ramanarayan, N. Pullanjiyot, and S. Swaminathan, Feather Like Highly Active Co_3O_4 Electrode for Supercapacitor Application: A Potentiodynamic Approach, *Mater. Res. Express*, 2018, **5**(6), p 065501
25. S. Vijayakumar, S. Nagamuthu, and G. Muralidharan, Supercapacitor Studies on NiO Nanoflakes Synthesized Through a Microwave Route, *ACS Appl. Mater. Interfaces.*, 2013, **5**(6), p 2188–2196
26. L. Zang, J. Zhu, and Y. Xia, Facile Synthesis of Porous NiO Nanofibers for High-Performance Supercapacitors, *J. Mater. Eng. Perform.*, 2014, **23**(2), p 679–683
27. T. Li, H. Yu, L. Zhi, W. Zhang, L. Dang, Z. Liu, and Z. Lei, Facile Electrochemical Fabrication of Porous Fe_2O_3 Nanosheets for Flexible Asymmetric Supercapacitors, *J. Phys. Chem. C*, 2017, **121**(35), p 18982–18991
28. L. Huang, D. Chen, Y. Ding, S. Feng, Z.L. Wang, and M. Liu, Nickel–Cobalt Hydroxide Nanosheets Coated on NiCo2O4 Nanowires Grown on Carbon Fiber Paper for High-Performance Pseudocapacitors, *Nano Lett.*, 2013, **13**(7), p 3135–3139
29. F. Qiu, L. Suo, W. Xiao, Z. He, Q. Du, and J. Chen, Few-Layer Graphene Functionalized by Carbon Nanotubes and MnO_2 Nanoparticles for High-Performance Supercapacitors, *J. Mater. Eng. Perform.*, 2019, **28**(7), p 4095–4101
30. V. Subramanian, S.C. Hall, P.H. Smith, and B. Rambabu, Mesoporous Anhydrous RuO_2 as a Supercapacitor Electrode Material, *Solid State Ion*, 2004, **175**(1), p 511–515
31. B. Xu, L. Pan, and Q. Zhu, Synthesis of Co3S4 Nanosheets and Their Superior Supercapacitor Property, *J. Mater. Eng. Perform.*, 2016, **25**(3), p 1117–1121
32. J. Hu, M. Noked, E. Gillette, F. Han, Z. Gui, C. Wang, and S.B. Lee, Dual-Template Synthesis of Ordered Mesoporous Carbon/Fe_2O_3 Nanowires: High Porosity and Structural Stability for Supercapacitors, *J. Mater. Chem. A*, 2015, **3**(43), p 21501–21510
33. M. Li, G. Sun, P. Yin, C. Ruan, and K. Ai, Controlling the Formation of Rodlike V_2O_5 Nanocrystals on Reduced Graphene Oxide for High-Performance Supercapacitors, *ACS Appl. Mater. Interfaces.*, 2013, **5**(21), p 11462–11470
34. S. Abouali, M. Akbari Garakani, B. Zhang, Z.-L. Xu, E. Kamali Heidari, J.-Q. Huang, J. Huang, and J.-K. Kim, Electrospun Carbon Nanofibers with in Situ Encapsulated Co_3O_4 Nanoparticles as Electrodes for High-Performance Supercapacitors, *ACS Appl. Mater. Interfaces*, 2015, **7**(24), p 13503–13511
35. S. Yang, Y. Liu, Y. Hao, X. Yang, W.A. Goddard, III, X.L. Zhang, and B. Cao, Cao, Oxygen-Vacancy Abundant Ultrafine Co_3O_4/Graphene Composites for High-Rate Supercapacitor Electrodes, *Adv. Sci.*, 2018, **5**(4), p 1700659
36. S. Jana, N. Singh, A.S. Bhattacharyya, and G.P. Singh, Synthesis of Self-Assembled rGO-Co_3O_4 Nanoparticles in Nanorods Structure for Supercapacitor Application, *J. Mater. Eng. Perform.*, 2018, **27**(6), p 2741–2746
37. J. Chen, N. Chen, X. Feng, and W. Hou, Preparation of Shape-Controlled Graphene/Co_3O_4 Composites for Supercapacitors, *J. Mater. Eng. Perform.*, 2016, **25**(9), p 3845–3851
38. Q. Guan, J. Cheng, B. Wang, W. Ni, G. Gu, X. Li, L. Huang, G. Yang, and F. Nie, Needle-like Co_3O_4 Anchored on the Graphene with Enhanced Electrochemical Performance for Aqueous Supercapacitors, *ACS Appl. Mater. Interfaces*, 2014, **6**(10), p 7626–7632
39. G. He, J. Li, H. Chen, J. Shi, X. Sun, S. Chen, and X. Wang, Hydrothermal Preparation of Co_3O_4@graphene Nanocomposite for Supercapacitor with Enhanced Capacitive Performance, *Mater. Lett.*, 2012, **82**, p 61–63

40. L. Ma, H. Zhou, X. Shen, Q. Chen, G. Zhu, and Z. Ji, Facile Synthesis of Co_3O_4 Porous Nanosheets/Reduced Graphene Oxide Composites and Their Excellent Supercapacitor Performance, *RSC Adv.*, 2014, **4** (95), p 53180–53187
41. L.-J. Xie, J.-F. Wu, C.-M. Chen, C.-M. Zhang, L. Wan, J.-L. Wang, Q.-Q. Kong, C.-X. Lv, K.-X. Li, and G.-H. Sun, A Novel Asymmetric Supercapacitor with an Activated Carbon Cathode and a Reduced Graphene Oxide–Cobalt Oxide Nanocomposite Anode, *J. Power Sources*, 2013, **242**, p 148–156
42. W. Xuan, R. Ramachandran, C. Zhao, and F. Wang, Influence of Synthesis Temperature on Cobalt Metal–Organic Framework (Co-MOF) Formation and Its Electrochemical Performance Towards Supercapacitor Electrodes, *J. Solid State Electrochem.*, 2018, **22**(12), p 3873–3881
43. R. Ramachandran, C. Zhao, D. Luo, K. Wang, and F. Wang, Morphology-Dependent Electrochemical Properties of Cobalt-Based Metal Organic Frameworks for Supercapacitor Electrode Materials, *Electrochim. Acta*, 2018, **267**, p 170–180
44. W. Xuan, R. Ramachandran, C. Zhao, F. Wang In *Synthesis of Hollow Nano-Structured Cobalt Metal–Organic Framework for Supercapacitor Electrodes*, 2018 IEEE International Conference on Manipulation, Manufacturing and Measurement on the Nanoscale (3M-NANO), 13–17 Aug. 2018; 2018; pp. 42–46
45. R. Ramachandran, K. Rajavel, W. Xuan, D. Lin, and F. Wang, Influence of $Ti_3C_2T_x$ (MXene) Intercalation Pseudocapacitance on Electrochemical Performance of Co-MOF Binder-Free Electrode, *Ceram. Int.*, 2018, **44**(12), p 14425–14431
46. Ü. Alver and A. Tanrıverdi, Boron Doped ZnO Embedded into Reduced Graphene Oxide for Electrochemical Supercapacitors, *Appl. Surf. Sci.*, 2016, **378**, p 368–374
47. X. Chi, L. Chang, D. Xie, J. Zhang, and G. Du, Hydrothermal Preparation of Co_3O_4/Graphene Composite as Anode Material for Lithium-Ion Batteries, *Mater. Lett.*, 2013, **106**, p 178–181
48. M. Endo, C. Kim, T. Karaki, T. Tamaki, Y. Nishimura, M.J. Matthews, S.D.M. Brown, and M.S. Dresselhaus, Structural Analysis of the B-Doped Mesophase Pitch-Based Graphite Fibers by Raman Spectroscopy, *Phys. Rev. B*, 1998, **58**(14), p 8991–8996
49. R. Naresh Muthu, S. Rajashabala, and R. Kannan, Hexagonal Boron Nitride (h-BN) Nanoparticles Decorated Multi-Walled Carbon Nanotubes (MWCNT) for Hydrogen Storage, *Renew. Energy*, 2016, **85**, p 387–394
50. J. Li, Z. Li, F. Ning, L. Zhou, R. Zhang, M. Shao, and M. Wei, Ultrathin Mesoporous Co_3O_4 Nanosheet Arrays for High-Performance Lithium-Ion Batteries, *ACS Omega*, 2018, **3**(2), p 1675–1683
51. L. Xu, Q. Jiang, Z. Xiao, X. Li, J. Huo, S. Wang, and L. Dai, Plasma-Engraved Co_3O_4 Nanosheets with Oxygen Vacancies and High Surface Area for the Oxygen Evolution Reaction, *Angew. Chem. Int. Ed.*, 2016, **55**(17), p 5277–5281
52. A.N. Naveen and S. Selladurai, Tailoring Structural, Optical and Magnetic Properties of Spinel Type Cobalt Oxide (Co_3O_4) by Manganese Doping, *Physica B Condens. Matter*, 2015, **457**, p 251–262
53. Y. Song, D.-Y. Feng, T.-Y. Liu, Y. Li, and X.-X. Liu, Controlled Partial-Exfoliation of Graphite Foil and Integration with MnO_2 Nanosheets for Electrochemical Capacitors, *Nanoscale*, 2015, **7**(8), p 3581–3587
54. W. Cheng, X. Liu, N. Li, J. Han, S. Li, and S. Yu, Boron-Doped Graphene as a Metal-Free Catalyst for Gas-Phase Oxidation of Benzyl Alcohol to Benzaldehyde, *RSC Adv.*, 2018, **8**(20), p 11222–11229
55. M. Zhang, Y. Wang, D. Pan, Y. Li, Z. Yan, and J. Xie, Nitrogen-Doped 3D Graphene/MWNTs Nanoframework-Embedded Co_3O_4 for High Electrochemical Performance Supercapacitors, *ACS Sustain. Chem. Eng.*, 2017, **5**(6), p 5099–5107
56. X. Tian, X. Sun, Z. Jiang, Z.-J. Jiang, X. Hao, D. Shao, and T. Maiyalagan, Exploration of the Active Center Structure of Nitrogen-Doped Graphene for Control over the Growth of Co3O4 for a High-Performance Supercapacitor, *ACS Appl. Energy Mater.*, 2018, **1**(1), p 143–153
57. J. Wang, J. Polleux, J. Lim, and B. Dunn, Pseudocapacitive Contributions to Electrochemical Energy Storage in TiO_2 (Anatase) Nanoparticles, *J. Phys. Chem. C*, 2007, **111**(40), p 14925–14931
58. Y. Jiang and J. Liu, Definitions of Pseudocapacitive Materials: A Brief Review, *Energy Environ. Mater.*, 2019, **2**(1), p 30–37
59. N. Elgrishi, K.J. Rountree, B.D. McCarthy, E.S. Rountree, T.T. Eisenhart, and J.L. Dempsey, A Practical Beginner's Guide to Cyclic Voltammetry, *J. Chem. Educ.*, 2018, **95**(2), p 197–206
60. S. Liu, S.C. Lee, U.M. Patil, C. Ray, K.V. Sankar, K. Zhang, A. Kundu, S. Kang, J.H. Park, and S. Chan Jun, Controllable Sulfuration Engineered NiO Nanosheets with Enhanced Capacitance for High Rate Supercapacitors, *J. Mater. Chem. A*, 2017, **5**(9), p 4543–4549
61. Z. Xiao, L. Fan, B. Xu, S. Zhang, W. Kang, Z. Kang, H. Lin, X. Liu, S. Zhang, and D. Sun, Green Fabrication of Ultrathin Co3O4 Nanosheets from Metal–Organic Framework for Robust High-Rate Supercapacitors, *ACS Appl. Mater. Interfaces.*, 2017, **9**(48), p 41827–41836
62. T.V. Nguyen, L.T. Son, V.V. Thuy, V.D. Thao, M. Hatsukano, K. Higashimine, S. Maenosono, S.-E. Chun, and T.V. Thu, Facile Synthesis of Mn-Doped $NiCo_2O_4$ Nanoparticles with Enhanced Electrochemical Performance for a Battery-Type Supercapacitor Electrode, *Dalton Trans.*, 2020, **49**(20), p 6718–6729
63. T. Wang, L.-X. Wang, D.-L. Wu, W. Xia, and D.-Z. Jia, Interaction between Nitrogen and Sulfur in Co-Doped Graphene and Synergetic Effect in Supercapacitor, *Sci. Rep.*, 2015, **5**, p 9591
64. D. Jain, J. Kanungo, and S.K. Tripathi, Performance Enhancement Approach for Supercapacitor by Using Mango Kernels Derived Activated Carbon Electrode with *p*-Hydroxyaniline based Redox Additive Electrolyte, *Mater. Chem. Phys.*, 2019, **229**, p 66–77
65. W. Zhou, J. Liu, T. Chen, K.S. Tan, X. Jia, Z. Luo, C. Cong, H. Yang, C.M. Li, and T. Yu, Fabrication of Co_3O_4-Reduced Graphene Oxide Scrolls for High-Performance Supercapacitor Electrodes, *Phys. Chem. Chem. Phys.*, 2011, **13**(32), p 14462–14465
66. R. Manikandan, C.J. Raj, M. Rajesh, B.C. Kim, J.Y. Sim, and K.H. Yu, Electrochemical Behaviour of Lithium, Sodium and Potassium Ion Electrolytes in a $Na_{0.33}V_2O_5$ Symmetric Pseudocapacitor with High Performance and High Cyclic Stability, *ChemElectroChem*, 2018, **5**(1), p 101–111
67. M. Jing, Y. Yang, Y. Zhu, H. Hou, Z. Wu, and X. Ji, An Asymmetric Ultracapacitors Utilizing α-$Co(OH)_2$/Co_3O_4 Flakes Assisted by Electrochemically Alternating Voltage, *Electrochim. Acta*, 2014, **141**, p 234–240
68. K.V. Sankar and R. Kalai Selvan, Improved Electrochemical Performances of Reduced Graphene Oxide Based Supercapacitor Using Redox Additive Electrolyte, *Carbon*, 2015, **90**, p 260–273
69. D.K. Kampouris, X. Ji, E.P. Randviir, and C.E. Banks, A New Approach for the Improved Interpretation of Capacitance Measurements for Materials Utilised in Energy Storage, *RSC Adv.*, 2015, **5**(17), p 12782–12791
70. C. Zheng, M. Yoshio, L. Qi, and H. Wang, A 4 V-Electrochemical Capacitor Using Electrode and Electrolyte Materials Free of Metals, *J. Power Sources*, 2014, **260**, p 19–26
71. C. Xiang, M. Li, M. Zhi, A. Manivannan, and N. Wu, A Reduced Graphene Oxide/Co_3O_4 Composite for Supercapacitor Electrode, *J. Power Sources*, 2013, **226**, p 65–70
72. G.K. Veerasubramani, K. Krishnamoorthy, P. Pazhamalai, and S.J. Kim, Enhanced Electrochemical Performances of Graphene Based Solid-State Flexible Cable Type Supercapacitor Using Redox Mediated Polymer Gel Electrolyte, *Carbon*, 2016, **105**, p 638–648
73. M.D. Levi, S. Sigalov, G. Salitra, R. Elazari, and D. Aurbach, Assessing the Solvation Numbers of Electrolytic Ions Confined in Carbon Nanopores under Dynamic Charging Conditions, *J. Phys. Chem. Lett*, 2011, **2**(2), p 120–124
74. R. Kumar, H.-J. Kim, S. Park, A. Srivastava, and I.-K. Oh, Graphene-Wrapped and Cobalt Oxide-Intercalated Hybrid for Extremely Durable Super-Capacitor with Ultrahigh Energy and Power Densities, *Carbon*, 2014, **79**, p 192–202
75. R. Wang, Q. Li, L. Cheng, H. Li, B. Wang, X.S. Zhao, and P. Guo, Electrochemical Properties of Manganese Ferrite-Based Supercapacitors in Aqueous Electrolyte: The Effect of Ionic Radius, *Colloids Surf. A Physicochem. Eng. Asp.*, 2014, **457**, p 94–99
76. K.V. Sankar, D. Kalpana, and R.K. Selvan, Electrochemical Properties of Microwave-Assisted Reflux-Synthesized Mn3O4 Nanoparticles in Different Electrolytes for Supercapacitor Applications, *J. Appl. Electrochem.*, 2012, **42**(7), p 463–470
77. Q. Qu, P. Zhang, B. Wang, Y. Chen, S. Tian, Y. Wu, and R. Holze, Electrochemical Performance of MnO_2 Nanorods in Neutral Aqueous Electrolytes as a Cathode for Asymmetric Supercapacitors, *J. Phys. Chem. C*, 2009, **113**(31), p 14020–14027
78. X. Zhang, X. Wang, L. Jiang, H. Wu, C. Wu, and J. Su, Effect of Aqueous Electrolytes on the Electrochemical Behaviors of Supercapacitors Based on Hierarchically Porous Carbons, *J. Power Sources*, 2012, **216**, p 290–296

79. A. Numan, N. Duraisamy, F. Saiha Omar, Y.K. Mahipal, K. Ramesh, and S. Ramesh, Enhanced Electrochemical Performance of Cobalt Oxide Nanocube Intercalated Reduced Graphene Oxide for Supercapacitor Application, *RSC Adv.*, 2016, **6**(41), p 34894–34902
80. T.T. Nguyen, V.H. Nguyen, R.K. Deivasigamani, D. Kharismadewi, Y. Iwai, and J.-J. Shim, Facile Synthesis of Cobalt Oxide/Reduced Graphene Oxide Composites for Electrochemical Capacitor and Sensor Applications, *Solid State Sci.*, 2016, **53**, p 71–77
81. Z. Song, Y. Zhang, W. Liu, S. Zhang, G. Liu, H. Chen, and J. Qiu, Hydrothermal Synthesis and Electrochemical Performance of Co_3O_4/Reduced Graphene Oxide Nanosheet Composites for Supercapacitors, *Electrochim. Acta*, 2013, **112**, p 120–126
82. H. Wang, Y. Shi, Z. Li, W. Zhang, and S. Yao, Synthesis and Electrochemical Performance of Co_3O_4/Graphene, *Chem. Res. Chin. Univ.*, 2014, **30**(4), p 650–655
83. F. Du, X. Zuo, Q. Yang, G. Li, Z. Ding, M. Wu, Y. Ma, S. Jin, and K. Zhu, Facile Hydrothermal Reduction Synthesis of Porous Co_3O_4 nanosheets@RGO Nanocomposite and Applied as a Supercapacitor Electrode with Enhanced Specific Capacitance and Excellent Cycle Stability, *Electrochim. Acta*, 2016, **222**, p 976–982
84. Y. Zou, I.A. Kinloch, and R.A.W. Dryfe, Mesoporous Vertical Co_3O_4 Nanosheet Arrays on Nitrogen-Doped Graphene Foam with Enhanced Charge-Storage Performance, *ACS Appl. Mater. Interfaces*, 2015, **7**(41), p 22831–22838
85. Y. Wang, R. Ma, L. Liu, Z. Xu, and F. Li, A Facile One-Pot Method for Co_3O_4/Graphene Composite as Efficient Electrode Materials for Supercapacitors, *Nano*, 2017, **12**(08), p 1750102
86. H.-W. Wang, Z.-A. Hu, Y.-Q. Chang, Y.-L. Chen, Z.-Y. Zhang, Y.-Y. Yang, and H.-Y. Wu, Preparation of Reduced Graphene Oxide/Cobalt Oxide Composites and Their Enhanced Capacitive Behaviors by Homogeneous Incorporation of Reduced Graphene Oxide Sheets in Cobalt Oxide Matrix, *Mater. Chem. Phys.*, 2011, **130**(1), p 672–679
87. S. Huang, Y. Jin, and M. Jia, Preparation of Graphene/Co_3O_4 Composites by Hydrothermal Method and Their Electrochemical Properties, *Electrochim. Acta*, 2013, **95**, p 139–145
88. Q. Li, X. Hu, Q. Yang, Z. Yan, L. Kang, Z. Lei, Z. Yang, and Z. Liu, Electrocapacitive Performance of Graphene/Co_3O_4 Hybrid Material Prepared by a Nanosheet Assembly Route, *Electrochim. Acta*, 2014, **119**, p 184–191